

POLITECNICO DI TORINO

Master's Degree in Aerospace Engineering



Master's Degree Thesis

Mid- to close-range relative navigation with a non-cooperating target in LEO using range and line of sight measurements

Supervisors

Prof. Lorenzo CASALINO

Prof. Manuela BATTIPEDE

Jean-Sébastien ARDAENS

Muriel RICHARD

Candidate

Filippo BARTOLINI

April 2020

POLITECNICO DI TORINO
ÉCOLE POLYTECHNIQUE FÉDÉRALE DE LAUSANNE



POLITECNICO
DI TORINO

EPFL

MASTER THESIS - M.S. AEROSPACE ENGINEERING

Mid- to close-range relative navigation
with a non-cooperating target in LEO
using range and line of sight measurements

Author:

Filippo Bartolini

Under the direction of

Prof. **Lorenzo Casalino** (PoliTo)

Prof. **Manuela Battipede** (PoliTo)

Jean-Sébastien Ardaens (DLR)

Muriel Richard (EPFL)

EPFL

Lausanne, April 2020

*Tu quamcumque deus tibi fortunaverit horam
grata sume mami neu dulcia differ in annum,
ut quocumque loco fueris vixisse libenter
te dicas; nam si ratio et prudentia curas,
non locus effusi late maris arbiter aufert,
coelum, non animum mutant, qui trans mare currunt.
Strenua nos exercet inertia; navibus atque
quadrigis petimus bene vivere. Quod petis, hic est,
est Ulubris, animus si te non deficit aequus.*

Horatius, Epistula XI

To my grandparents

Acknowledgements

First of all I wish to thank my supervisor, Jean-Sébastien Ardaens, for his mentoring. Despite the distance and the many commitments, he managed to follow me and accompany me in my work throughout these months. I'm grateful for the learning opportunities he has given me, and for beginning to teach me how to look at problems from an engineering perspective.

Thanks to those who welcomed me in the EPFL—the people of eSpace and ClearSpace—for making me feel included right from the start and for always offering their help. Prof Jean-Paul Kneib and Muriel Richard first. And then Bastien, Candice, Michaël, Jacques, Alex, Marc-André, Noemy, Mohammad, Charles, Emmanuelle, Hannes, Simon, John, Andrew, prof. Kneib, Brigitte, Reyhaneh, and my office mates Elisa and Flavio, for the everyday company during these months.

I'm grateful for my professors from PoliTo, prof. Casalino and prof. Battipede, for their continuous availability and support.

Thanks to the friends I found in Lausanne, primarily those whom I live with. To all of them for making it possible to feel at home while being away from it.

To all my friends from Torino —with whom I shared everyday life all through these last years— it would be impossible to list them all. To Poli and suorine above all: thanks to them I realized how wonderful it is to be supported in our yearning to grow and our commitment to study.

My gratitude also to Simona. For her firm support, closeness and holy patience.

At last, to my family, who is always pushing me to look for the essential things. To them, and especially to my mother, I dedicate the conclusion of my university *iter*.

Abstract

Space debris represents a more and more growing problem for space operations, especially for spacecrafts operating in Low Earth Orbit (LEO), that proves to be the most crowded region in terms of orbiting objects. In the very last years, many actors in space economy started to be concerned about this issue and the main solution seems to be the Active Debris Removal (ADR). It is better to force the orbital decay process of an object instead of letting it to deorbit by itself in some decades. This is a reasonable way to face the constantly increasing of spacecrafts number and debris population. This thesis has been conducted within a start-up, Clear Space, born from the EPFL Space Center, that is facing the challenge of designing an ADR mission for the European Space Agency in order to remove a specified object. The main challenge in ADR is about non-cooperation aspect. While a well-known classical rendezvous is performed by two active players, in a non-cooperative rendezvous one of the two objects does not actively take part in the operation. For this reason, the other spacecraft, the chaser, must be able to perform the task by itself. Another crucial point is the autonomy. Since the operations are executed in close-proximity, it has to be also able to detect a risk of collision or to decide to correct the formation and perform maneuvers without waiting for ground commands. On-board sensors and computations gain therefore much importance. So far, technologies for relative navigation has been commissioned and tested and Angles Only Navigation (AON) provide a simple and safe mean to perform far-to mid-range approach. In order to perform closer-range navigation and formation keeping, line-of-sight navigation is not enough and the knowledge of the range should be provided. A line-of-sight and range based Guidance, Navigation and Control (GNC) system is presented, as a development of the in-flight heritage of AON. A simplified dynamical model is used to gather measurements of relative position. The purpose of this study is to understand how well range measurements may improve the state estimation and control loop. Different scenarios are then simulated for mid- to close-range formation reconfiguration and close-range formation keeping.

Keywords

Space debris, relative motion, relative orbital elements, non-cooperative rendezvous, impulsive manoeuvres, Kalman filtering.

Contents

Acronyms

Nomenclature

1	Introduction	1
1.1	About space debris	1
1.2	Recent events	3
1.2.1	Anti-satellite tests	4
1.2.2	Iridium 33/Kosmos 2251 collision	5
1.2.3	Sentinel-1A debris impact	6
1.2.4	Collision countermeasures and spacecrafts' autonomy	7
1.3	Active Debris Removal	9
1.3.1	Need for ADR	10
1.3.2	Efficiency of ADR activities	12
1.3.3	Sun synchronous orbits	12
1.3.4	Polar hotspots	13
1.3.5	Non cooperative rendezvous	14
1.4	State of the art	16
1.4.1	PRISMA	16
1.4.2	TanDEM-X	17
1.4.3	AVANTI	18
1.4.4	CleanSpace One	20
1.5	ClearSpace	21
1.5.1	VESPA adapter	22
2	Fundamentals	25
2.1	Orbital dynamics	26
2.1.1	Unperturbed relative motion	29
2.1.1.1	Hill's equations	31
2.1.1.2	Relative Orbital Elements	33
2.1.2	Perturbed relative motion	38
2.1.2.1	Gravitational field	38

2.1.2.2	Differential drag	41
2.2	Relative state control	44
2.2.1	Control strategy	45
2.2.2	Passive safety	48
2.3	Estimation	49
2.3.1	EKF formulation	49
2.3.2	Measurement model	51
3	Simulation environment	54
3.1	simulation baseline	54
3.2	Images generation	56
3.3	Range measurements	57
3.4	Maneuver execution errors	58
4	Simulation results	59
4.1	Convergence	59
4.2	formation reconfiguration and keeping	59
4.3	Out-of-plane: no fast convergence	63
4.4	Covariance, P	65
4.5	Recommendations	65
4.6	Further development	65
A	Control algorithm	66
B	EKF algorithm	70
C	Close formation keeping	72

List of Figures

1.1	Growth trend of man-made objects in all orbits since the beginning of space era [1]	2
1.2	Growth trend of objects in different orbits [1]	3
1.3	evolution of objects in LEO.	4
1.4	Fengyun-1C debris cloud	5
1.5	View of Iridium 33 and Kosmos 2251 Orbits at Time of Collision	6
1.6	Comparison of the interested area on the solar array, before and after the impact (credits ESA)	7
1.7	A radar image of Envisat	11
1.8	Forecast debris density at poles pillars	13
1.9	Gemini 7 spacecraft seen from Gemini 6 during their rendezvous, December 1965 (credits NASA)	14
1.10	Astronauts of STS-49 handling Intelsat 603 satellite (credits NASA)	15
1.11	GPS-based relative distance between Mango and Tango over time, up to December 31, 2011.	17
1.12	Spiral relative trajectory	19
1.13	Measurements during the close-range approach	20
1.14	Artistic illustration of the "Pac-Man" configuration for CleanSpace spacecraft (credits EPFL)	20
1.15	ClearSpace logo	22
1.16	VEGA payload bay and one fairing.	23
2.1	ECI and ECEF frames	27
2.2	Mean and true anomaly	27
2.3	RTN frame, centered in chief satellite	30
2.4	Eccentricity factor	33
2.5	chief's and deputy's eccentricity vectors on chief's perifocal plane	35
2.7	Along-track drift due to a non-zero relative semi-major axis	36
2.6	Relative trajectory projections on RT and RN planes [2]	36
2.8	Perturbing accelerations in Earth orbits [3]	38
2.9	Relative eccentricity and relative inclination vectors variations [2]	41
2.10	Atmospheric density	43

2.11	Drift within a control period	47
2.12	Tolerance windows for relative eccentricity and relative inclination . .	48
2.13	Predictor-corrector EKF loop	50
2.14	RTN frame and relative position	51
2.15	Block scheme of the filter's measurement model	53
3.1	High level simulation environment layout	55
3.2	Examples of generated images and computed centroids	56
3.3	Misaligned centroid: maximum angular error seen by the on-board camera	57
3.4	Maneuver execution error: $\Delta \mathbf{v}$ uncertainty sphere	58
4.1	Convergence during the initial period (18000 s, about 5 hours)	60
4.2	scenario 01, ROE evolution	61
4.3	scenario 01, error	62
4.4	scenario 01, residuals	62
4.5	Covariance envelop amplitude for each ROE	64
A.1	Control algorithm flowchart	67
A.2	In-plane control	68
A.3	Out-of-plane control	69
B.1	Extended Kalman Filter data flow.	71
C.1	scenario 02, error	73
C.2	scenario 02, residuals	73
C.3	scenario 02, error	74
C.4	scenario 02, residuals	74

Acronyms

AON Angles Only Navigation.

AVANTI Autonomous Vision Approach Navigation and Target Identification.

ECEF Earth Centered Earth Fixed.

ECI Earth Centered Inertial.

EGO Extended Geostationary Orbit.

EKF Extended Kalman Filter.

EPFL École polytechnique fédérale de Lausanne.

ESA European Space Agency.

GEO Geostationary Orbit.

GNC Guidance, Navigation and Control.

GPS Global Positioning System.

GTO GEO Transfer Orbit.

HEO Highly Eccentric Earth Orbit.

KOE Keplerian Orbital Elements.

LEO Low Earth Orbit.

LMO LEO-MEO crossing orbits.

LOS Line-Of-Sight.

LVLH Local Vertical Local Horizontal.

MEO Medium Earth Orbit.

MGO MEO-GEO crossing orbits.

NASA National Aeronautics and Space Administration.

NSO Navigation Satellites Orbits.

PRISMA Prototype Research Instruments and Space Mission technology Advancement.

ROE Relative Orbital Elements.

RTN Radial-Transverse-Normal.

STS Space Transportation System.

TAFF TanDEM-X Autonomous Formation Flying.

TLE Two Lines Element.

VESPA VEGA Secondary Payload Adapter.

Nomenclature

Physics Constants

μ	Earth's gravitational parameter	$3.986004418 \times 10^{14} m^3 s^{-2}$
G	Universal gravitational constant	$6.67408 \times 10^{-11} m^3 s^{-2} kg^{-1}$
J_2	Geopotential second-order zonal coefficient	0.00108263
m_{\oplus}	Earth's mass	$5.9722 \times 10^{24} kg$
R_{\oplus}	Earth's equatorial radius	$6.3781370 \times 10^6 m$

Symbols

$\Delta \mathbf{v}$	Velocity increment after impulsive thrust
ρ	Atmospheric density
m_j	j-th spacecraft's mass
u	Mean argument of latitude

Chapter 1

Introduction

A collision in Low Earth Orbits could easily happen with a relative velocity of about 10 km/s. Such an event must be avoided as much as possible by every spacecraft. Nevertheless, new objects are brought in space far faster than the expired ones are removed. For this reason, the population of objects in Earth orbits is constantly growing, mainly thank to less and less expensive ways to insert spacecrafts in orbit and the spreading of companies able to launch rockets by themselves.

On the one hand, such improvements lead to the benefit of a broader access to space for any kind of purpose (education, science, weather forecast, surveillance, communications, human space exploration, only to cite the most common), on the other hand the increasing unconstraint risk of having collision among spacecrafts or between spacecrafts and debris: the latter occurrence is less predictable than the first.

1.1 About space debris

After 60 years of space launches, about 8000 tons of material have been inserted in near-Earth orbits. Among this, about 6300 tons are dead satellites and debris in general. Even by stopping launching everything today, the debris population will inexorably grow due to the collisions that will occur among them, sooner or later. A collision of two objects may generate thousands of debris, which can collide with other objects, in a sort of chain process. By the end of the seventies, this phenomenon started to concern space users: nowadays, it is very common to hear about the “Kessler syndrome”, named after the debris scientist Donald Kessler, who proposed this dramatic scenario [4].

Nowadays, LEO region hosts more than 2/3 of the overall debris number. Since LEO extends to a height of about 2000 km above the Earth’s surface, it follows that the very near-Earth region is full of both operating and dead satellites and any kind of debris. In general, almost 7% of the monitored objects in space are composed

of functional satellites, that is nearly 2000 satellites. ESA estimates that currently there are more than 30 thousand objects bigger than 10 cm. The number of objects is fastly increasing and all this junk is causing a major risk to spaceflight. When disused, satellites may explode or collide with other objects, then break up into smaller pieces of all shapes and sizes, many of which measure less than 10 cm across and are undetectable from Earth. According to the ESA's annual space environment report [1], about 5000 thousand of all satellites ever launched since the beginning of the space era in 1957 are still in orbit. About 1950 of them are functioning. Today, more than 20000 objects are present in all Earth orbits and among half of them are the result of fragmentation events. Fragmentation is the most dangerous event that can occur because, in addition to the loss of the object itself (that could be a payload or just a used rocket body), it gives birth to a myriad of highly dangerous objects. About 10000 objects have been produced by accidental explosions of launch vehicles, mainly due to the unused fuel remained inside the rocket body. Therefore, it is clear that dismissed payloads, rocket bodies and any other object that is not under direct control represent a serious potential source of debris other than a concrete risk of collision. For clarity purposes, it is enough to pay attention to the graphs from ESA's report showing the evolution of the environment in orbit. Figure 1.1 shows the evolution in time of the population in all Earth orbits -i.e. from LEO to GEO and HEO, cataloguing the objects by type.

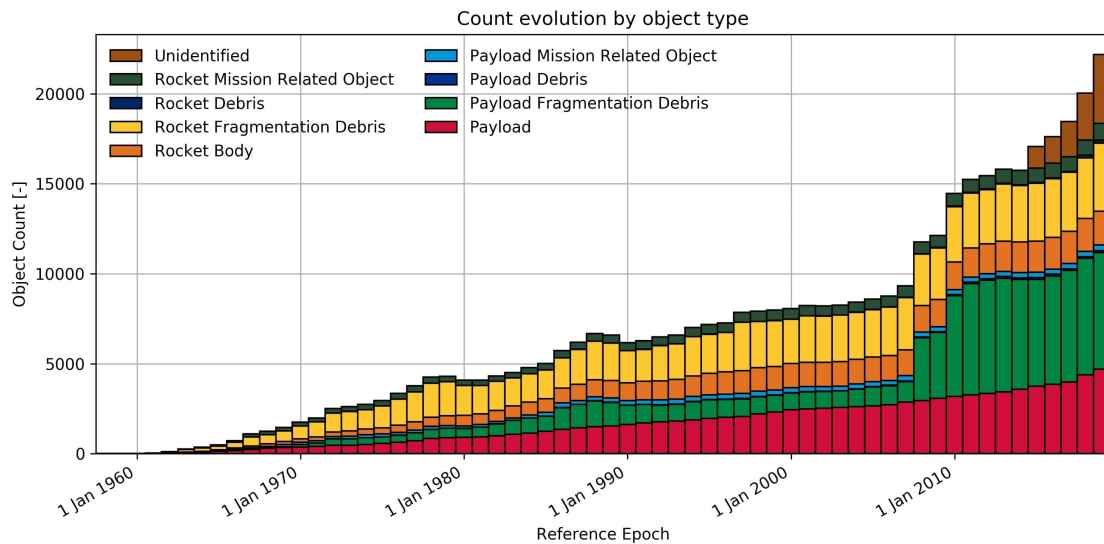


Figure 1.1: Growth trend of man-made objects in all orbits since the beginning of space era [1]

1.2 Recent events

In Figure 1.1, one can notice two steps in the green bars trend (payload fragmentation debris), in the neighborhood of the year 2010. These two wider steps correspond to as much fragmentation events, happened in 2007 and 2009. Debris impacts may occur, and it may damage in many ways a spacecraft (from a scratch to the total loss of the satellite). A debris is often a manmade object or even the result of an event such as fragmentation, or a natural body – as micrometeorites. The smaller the debris, the more difficult the prevention. With the increasing number of objects in orbit, space agencies are often forced to take countermeasures to avoid collisions with debris or even with another spacecraft.

Figures 1.2 and 1.3 shows the same evolution, with respect to different orbit types, and the trend of penetration into LEO (i.e. both LEOs themselves and orbits with a very low perigee).

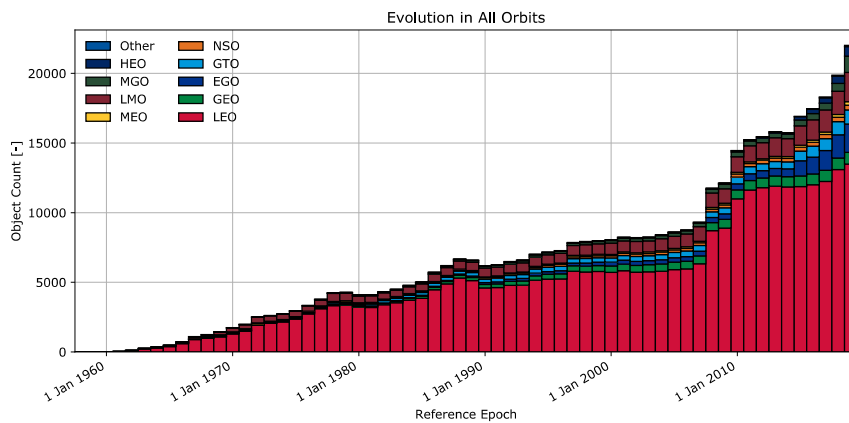


Figure 1.2: Growth trend of objects in different orbits [1]

(see Acronyms list for: HEO, MGO, LMO, MEO, NSO, GTO, EGO, GEO, LEO)

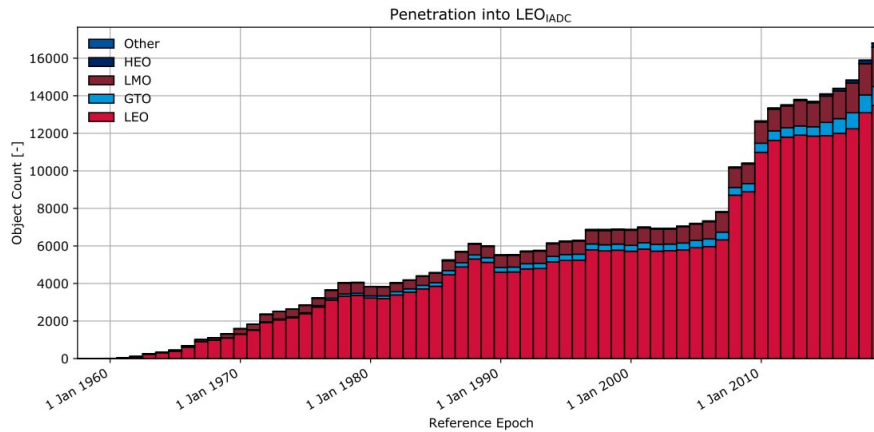


Figure 1.3: evolution of objects in LEO.

Amount of objects penetrating into LEO protected region (below 2000 km altitude), defined by Inter-Agency Space Debris Coordination Committee (IADC) [1].

1.2.1 Anti-satellite tests

On January 11, 2007, China launched a ballistic missile targeting a non-operational Chinese weather Fengyun-1C satellite in Sun-synchronous orbit, as an anti-satellite test [5]. The collision created a cloud of thousands of pieces and spread out from a limited region as of the event occurrence to several LEO orbits. Obviously, such a spread cloud of debris represented a high risk for LEO satellites, and mainly for the International Space Station. As an example, some months after the event, in June 2007, the NASA's TERRA satellite executed a maneuver to avoid a 7% chance of being struck by the new-born cloud. The importance of this event mainly lies in the satellite altitude, about 860 km: the higher the altitude where a collision occurs, the longer the debris clouds will stay in orbit. Figure 1.4 shows the evolution in time of the cloud, from few minutes after the collision up to three years after.

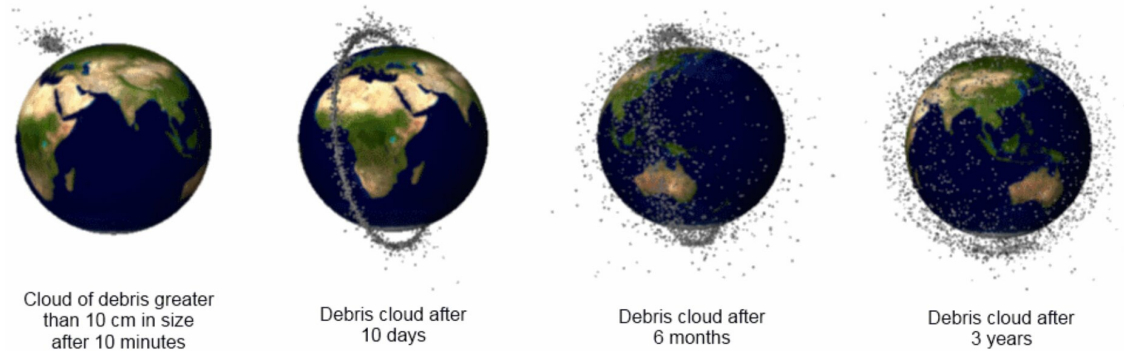


Figure 1.4: Fengyun-1C debris cloud

Estimation, after three years, of the evolution of the debris cloud generated by the 2007 satellite kinetic kill [6]. Nowadays, part of the debris cloud is still in orbit and TLE data are available

Although this episode represents the most recent and the one that produced the largest debris cloud, many other anti-satellite tests have been carried out in precedent years. Countries as USA, Russia, and India developed antisat weapons too but, for what concerns the known tests made, impacts usually have happened at low altitudes, approximately below 500 km, and the clouds of debris burned in the atmosphere in some months [5] [7].

1.2.2 Iridium 33/Kosmos 2251 collision

Two years later, on February 10, 2009, the first accidental collision between two satellites occurred [8]. The event took place above Siberia, at a height of about 800 km and a relative velocity of about 11.7 km/s and involved a communication satellite belonging to the US's constellation Iridium, Iridium 33, and an inactive Russian communication satellite, Kosmos 2251. This was therefore the first case an operational satellite hit a dismissed one [9]. Two clouds of debris were generated and most of the pieces are still in orbit. It is important to consider that the result of such a collision was two different debris clouds, essentially laying on the two satellites orbits. The occurrence of the collision above the North Pole is not fortuitous. Since polar orbits are used for a multitude of operations (weather forecast, Earth mapping, observation. . .), crowded crossroads above poles are a direct consequence. This topic will be treated in Section 1.8. Figure 1.5 shows the location of the collision.

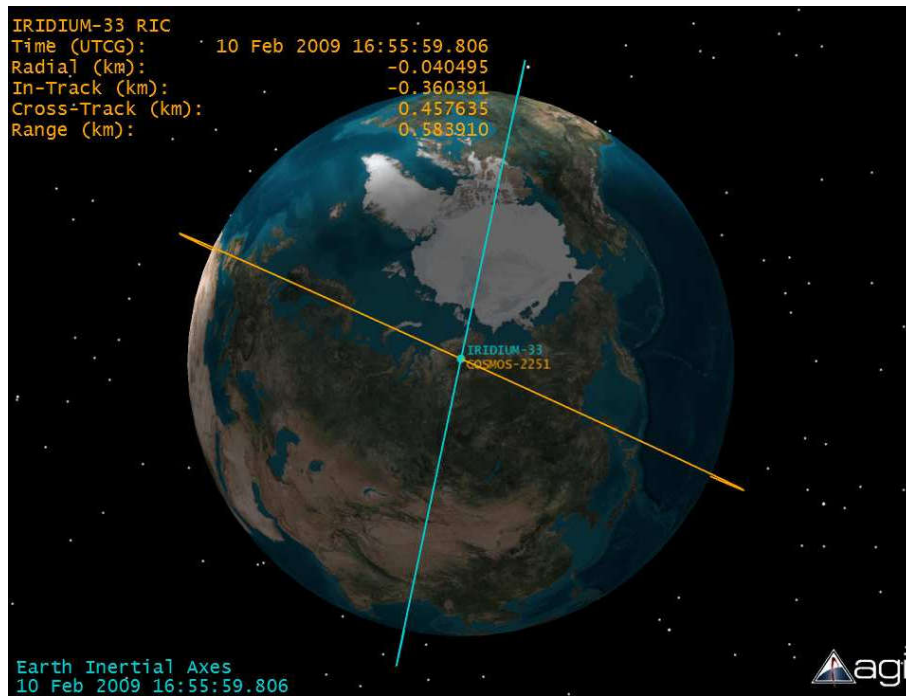


Figure 1.5: View of Iridium 33 and Kosmos 2251 Orbits at Time of Collision

This image belongs to the analysis described in [10], performed some months after the event. The geographic location above the North Pole can be seen

1.2.3 Sentinel-1A debris impact

In more recent times, on August 23, 2016, a debris impacted with the satellite Copernicus Sentinel-1A. After been diagnosed, it was classified as a millimeter-sized particle and the episode did not produce serious consequences. The event was detected because of the sudden power loss of the solar panel hit by the particle happened in concurrence with a slightly change in satellite orientation. After on-board camera observation and analyses on the spacecraft's status, before and after that occurrence, investigations led to the conclusion of an impact with a particle of few millimeters, either of natural origin or man-made [11]. The impact left a damaged region of about 40 cm in diameter on solar array surface, recognizable in Figure 1.6, and the registered power loss of 280W, from the nominal 6000W, was permanent.

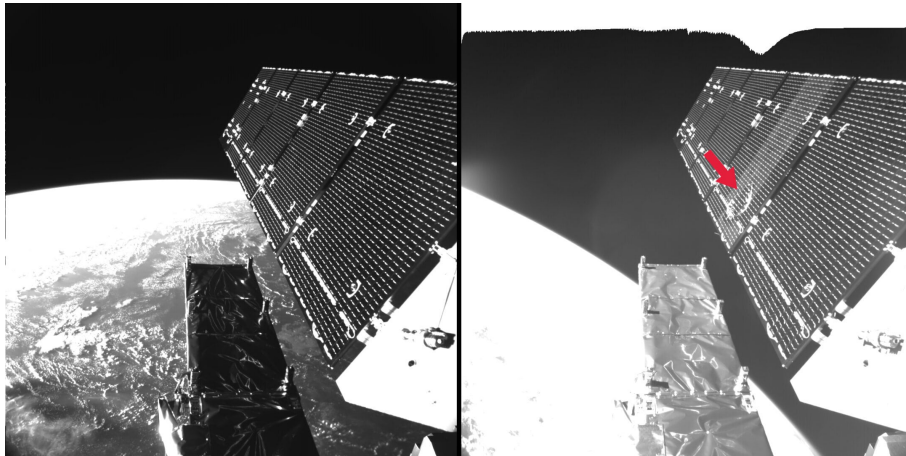


Figure 1.6: Comparison of the interested area on the solar array, before and after the impact (credits ESA)

It was a strike with a particle -for which it is impossible to know the exact origin, natural or manmade-, but one among the thousand's of pieces generated by the aforementioned events could have had the same effect. Such impacts may generate damages of different magnitude. For Sentinel 1A the particle caused the loss of a portion of a solar array but, with a greater size of the object, the damage may easily have been more serious than a partial reduction of the available electric power.

1.2.4 Collision countermeasures and spacecrafts' autonomy

The events so far described do not depict a scenario in which operational spacecrafts have no possibility to avoid debris, if it has been detected. The fact that a spacecraft should have been able to execute a maneuver in order to avoid a collision was clear since the 70's and 80's. The first confirmed, unintentional collision between two catalogued orbits occurred in 1996, between the French Cerise satellite (95-033B) and a fragment (86-019RF) of an Ariane-1 H-10 upper stage that exploded on 13 November 1986. The debris severed the gradient boom of the satellite [12].

In order to be able to successfully avoid a probable collision in time, the spacecraft needs a proper propulsion system but, first of all, it is essential to be aware of the objects that it may meet along its orbital path. This issue is not a problem if the object is a functional spacecraft too, of which both position and velocity are known. Therefore, the possibility of performing such maneuvers strongly depends on the capability of tracking non-operational objects, such as debris and dismissed satellites. With the even more increasing number of orbiting objects and the current capability of debris tracking, anti-collision maneuvers occur more frequently. Performing a maneuver begins to be considered if the probability for two objects to collide is greater than 10^{-3} [12]. Nowadays, space agencies constantly monitor their

own satellites, continuously evaluating the risk of collision with other objects and then scheduling maneuvers, if needed. For seek of completeness, collision avoidance procedures can be deepened in [13] and [14].

The need for routine debris monitoring is by now essential. Moreover, the growing orbit traffic, especially in LEO regions, generates a very huge amount of data. This makes the need for spacecraft's autonomy essential, in order to be able to manage collision risk situations autonomously.

Even if each one of the aforementioned events did not concern directly an actual collision among two spacecraft, the even higher collision risk deriving from the increasing population is a straightforward conclusion. Even by tracking every single debris in orbit – even those smaller than 1 cm-, most of them will however still represent a potential source for other debris. By recalling that about 18% of the cataloged objects in space are spent upper stage and mission-related objects (such as adapters) and that more than 290 in-orbit fragmentation events have been recorded since 1961, it clearly comes out how debris will continue to represent an annoying and dangerous obstacle.

Moreover, the need for even more frequent collision avoidance maneuvers suggests to pay attention to the upcoming theme of mega-constellations. In recent years, big companies as SpaceX, OneWeb, Amazon and many others, have announced their intent to create their own constellations, in order to spread high-speed internet all around the world. Such constellations will count hundreds and thousands of spacecrafts orbiting LEOs. Considering the present number of satellites in LEO, insertion of thousands of new satellites would represent a notable increasing of the risk of collision: Starlink constellation by SpaceX would count around 4000 satellites of about 200kg each, having started with orbit insertion in 2018, OneWeb more than 600, started in 2019, Amazon more than 3000 from 2022, and so forth with many other constellations, counting hundreds of satellites each, planned for launch in the next decade. Probably most of these missions won't see the light but what is sure is the future crowding projection. A helpful resource is that new satellites must be designed with precise end-of-life criteria in order to perform safe disposal. But also with this kind of mitigation, such constellations will populate an environment that already sees the presence of many debris and objects. From this, the need to be able to actively remove a not-functioning satellite or even only be able to guarantee a capacity of in-orbit servicing by means of a spacecraft without crew.

1.3 Active Debris Removal

LEO is the easier orbit to reach but it is also the orbit where atmosphere drag still exerts a non negligible contribution. Satellites in lower orbits are slowed down by the effect of upper atmospheric drag and gradually decay into the atmosphere itself until they burn. But even with this factor, a satellite would take some decades before it completely deorbits. Of course, higher orbits can't even count on drag. Thinking about Geostationary orbits, nowadays only graveyard orbits are considered as a suitable solution for dead satellites, since it is too expensive to make something deorbit from there. Going back to LEOs, this region is crucial both for the wide spectrum of applications and users, since these are the easiest orbit to reach, and because it is a necessary path to go further.

The servicing vehicle can be provided with a capture system (a robotic arm, clamps, a net...) in order to fasten the target and to be able to drag it and lowering its orbit. Even "passive" methods could be followed in order to "actively" remove a debris, without getting directly in touch with the target. For instance, the vehicle could install on the target a kit for deorbiting such as a solid rocket motor or an atmospheric drag sail, or even project ion beams to the surface of the target in order to slow it down. The main goal of ADR is to accelerate the deorbiting of the target. This could also imply that the chaser can carry the target to a lower orbit and then continue, without deorbit with it.

On overall orbits scale, ESA's estimates that fragmentations happen on average 5 times per year [15]. If no countermeasures will be taken and if the launch rate will remain the same as present day, in about a century the collision rate will be 25 times what it is now, making space flight very impracticable and the access to LEO almost impossible (ESA source). In the last years, the satellite's passivation has become part of the mission design. This is a good conduct for all the missions to come, in order to deorbit the satellite once its mission is over. Guidelines recommend to accomplish the complete removal within a time interval of 25 years [16]. Passivation methods have been already improved and applied in recent missions but, although it is a very practical and safe limitation to the growth of debris, it does not prevent it. There is already enough existing debris in space to represent a very high risk of cascade collisions. For older satellites, such as ENVISAT (launched in 2002 and still orbiting in an SSO), or in case of failure of a satellite before the end of life activities can be accomplished, passivation is not an option anymore and ADR is necessary. but Active Debris Removal missions are still in design phase and no in-orbit demonstration has been performed by a servicing vehicle yet. ESA, as a space technology and operations agency, has identified active removal technologies as a strategic goal. ADR seems to be the only long-term good solution for ensuring the space flight in current conditions will remain the same in the future and guaranteeing a 'business as usual' continuity.

1.3.1 Need for ADR

To actively remove a debris means that a service vehicle, a *chaser* from now on, needs to head itself physically in proximity of the debris, the *target*, in order to modify its orbit and help it in deorbiting. To perform such tasks implies many technical problems to solve. First, the chaser must approach an uncontrolled target and here lies the aspect of non-cooperation. A primary need stands therefore in collision avoidance: the chaser could collide with the target by intercepting its path (as Iridium and Kosmos did), but also by being hit by some part of the target's spinning body during the approach phase, due to different relative attitude of the two objects. Since no telemetry can be provided for the debris, neither the exact position and velocity or the actual attitude can be determined from the target itself. A target tracking from ground -by means of TLE data or direct ground observations- is indeed mandatory, in order to let the chaser reach the correct position of the target. But then the final approach needs to be performed in an autonomous way by the chaser, like a traditional rendezvous although with only one active player.

As one may easily notice, it is possible to track debris from ground, even very small ones. Indeed, specific telescopes can follow objects bigger than 10 cm and even some smaller ones. Space object catalogs, as generated and maintained by space surveillance networks, are limited to larger objects, typically greater than 10 cm in LEO (LEO, below 2000 km) and greater than 0.3–1 m in GEO (about 36 000 km). These sensitivity thresholds are a compromise between system cost and performance.

While telescopes are mainly suited for GEO and high-altitude debris observations, radars are advantageous for LEO [17]. Nowadays, a very large number of objects is constantly tracked and TLE data report real time day by day information about thousands of orbiting bodies. Therefore, it is possible to know position and velocity of a debris from ground.

In an ADR mission, the relative navigation close to the target has a primary role in making the closing and the rendezvous possible. After having roughly reached the target orbit, the chaser must track the target precisely in order to perform the final approach and then reduce and phase the relative spin. As long as the aim is to be roughly aware of where non-cooperative objects are, ground observations are sufficient but, if the aim is the relative navigation, then one needs something more reliable.

Main obstacles related to ground-based navigation are:

- the motion of the observed object is well described for what concerns the *in-plane* component -i.e. components of position and velocity vectors laying on the orbital plane- but not for the *cross-track* direction either -i.e. the direction perpendicular to the orbital plane.
- Limited period of observability: a radar can track a spacecraft in LEO for a

relatively short time, 5 to 20 minutes before it disappears again beyond the horizon, and this period strongly depends on the terrain mesh around the ground station. This would imply a long period of inactivity per orbit for the chaser;

- The resolution of the image returned by the radar may be not detailed enough to ensure a safe approach. (as an example, Figure 1.7 shows a radar image of Envisat satellite)

It is important to note that even if the ground measurements were perfect, it would take time for the signal sent from the ground station to reach the chaser. This would imply a delay in the estimation-control loop and the impossibility to know the relative state target-chaser at the current time. Indeed, in order to quantify this latency, the transit time for a round trip to a satellite in LEO and back is about 30 to 50 milliseconds [18].

Therefore, objects in LEO with a characteristic dimension at level of 1 meter can be trackable relatively easily from ground. But the target orbit provided by such observations is not enough. The close-range navigation -i.e. below 50 meters of relative distance- and the final approach cannot be safely performed by only mean of ground observations. In order to do close-proximity operations, the chaser must **sense** the target, **estimate** the relative state, **compute** a guidance plan and **control** the relative position autonomously.

The system presented in the present study shall allow a coarse formation keeping, which will be used to validate and commission more advanced relative navigation systems, which are necessary for the capture. This concept will be deepened in Chapter 3.

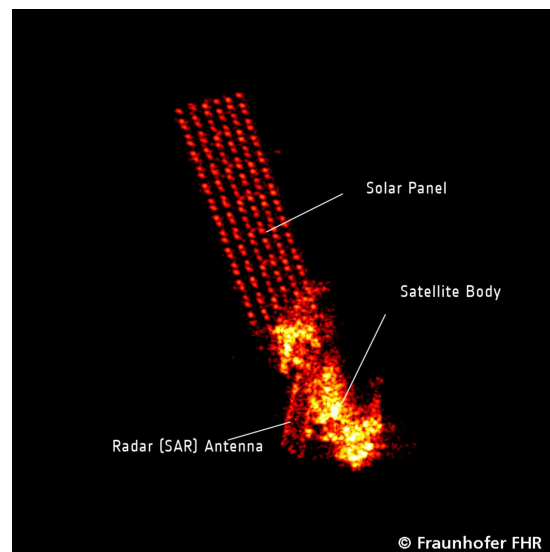


Figure 1.7: A radar image of Envisat

This radar image was produced by the ground-based tracking and imaging radar, TIRA, of the Fraunhofer Institute for High Frequency Physics and Radar Techniques in Wachtberg, Germany, on 10 April 2012.

1.3.2 Efficiency of ADR activities

Active removal can be more efficient in terms of the number of collisions prevented versus objects removed when the following principles are applied for the selection of removal targets, which can be used to generate a criticality index and the according list:

- The selected objects should have a high mass (they have the largest environmental impact in case of collision);
- Should have high collision probabilities (e.g. they should be in densely populated regions and have a large cross-sectional area);
- Should be in high altitudes (where the orbital lifetime of the resulting fragments is long).

Long-term environment simulations can be used to analyze orbital regions that are hotspots for collisions. The most densely populated region in LEO is around 800–1000 km altitude at high inclinations. The collision hotspots can be ranked by the number of collisions predicted to occur under a business as usual scenario. The most crucial regions among LEOs are those corresponding to the Earth poles. As seen for the collision between Iridium 33/Kosmos 2251, regions above Earth poles are crossroads for many satellites path in LEOs.

1.3.3 Sun synchronous orbits

The SunSynchronous Orbits, SSO, are a family of polar orbits. As the name suggests, polar orbits pass over the Earth's polar regions from north to south and viceversa. The orbital track of the satellite does not have to cross the poles exactly for an orbit to be called polar, an orbit which passes within 20 to 30 degrees of the poles is still classed as a polar orbit. These orbits mainly take place at low altitudes of between 200 to 1000 km. Satellites in polar orbit look down on the Earth's entire surface and can pass over the North and South Poles several times a day. Polar orbits are used for reconnaissance and Earth observation mainly. If a satellite is in polar orbit at an altitude of 800 km, it will be travelling at a speed of approximately 7.5 km per second.

A spacecraft in SSO has an orbital period synchronized with the Sun and therefore it passes over any given point on Earth's surface at the same local solar time. A satellite in a sun synchronous orbit would usually be at an altitude of between 600 to 800 km. Generally, these orbits are perfect for remote sensing, especially used for Earth observation, solar study, weather forecasting and reconnaissance, as ground observation is improved if the surface is always illuminated by the Sun at the same angle when viewed from the satellite.

1.3.4 Polar hotspots

Polar orbits in general assure to cover all Earth surface in few revolutions and SSOs are used for almost every remote sensing mission in LEO. It goes without saying that Earth Poles are crowded. According to ESA , high-ranking hotspot regions are at around:

- 1000 km altitude and 82 deg inclination;
- 800 km altitude and 98 deg inclination;
- 850 km altitude and 71 deg inclination.

The concentration of critical-size objects in these narrow orbital bands could allow multi-target removal missions. Such missions could be specifically designed for one orbit type were several objects of the same type are contained.

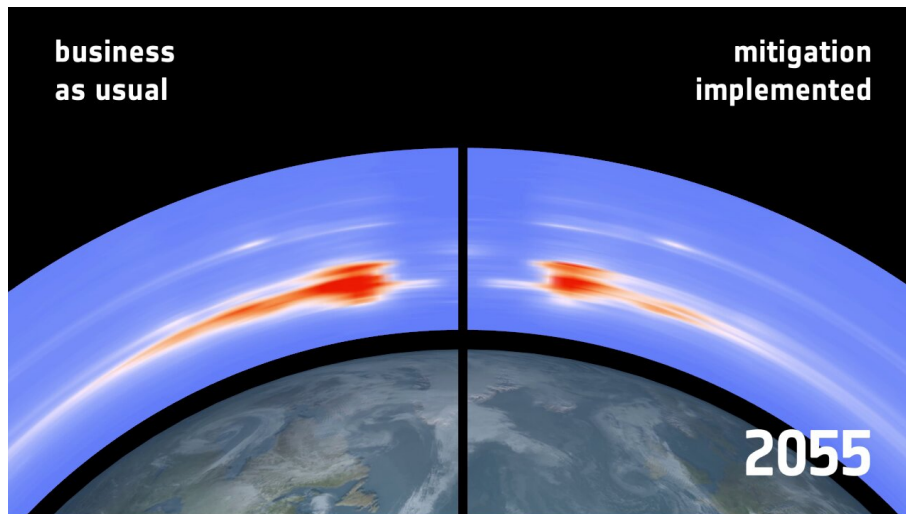


Figure 1.8: Forecast debris density at poles pillars

The image shows a forecast for 2055: on the left, a business-as-usual scenario while, on the right, the same forecast with debris mitigation measures implemented starting in 2020 (credits *ESA*)

Actions to counter the exponential growth of space debris, such as mitigation and active removal, are most effective when they are applied as soon as possible. The further the number of critical intact objects in the environment deviates from a sustainable level, the more objects will have to be removed to suppress any additional growth and the multiplying effects thereof. ESA’s internal studies have shown that continuous removal actions starting in 2060 will only have 75% of the beneficial effect compared to an immediate start. As one can notice from Figure 1.8, the debris density at poles is supposed to increase widely by 2055 if no countermeasure will be taken. On the other hand, ESA’s forecast shows that a mitigation of this crowding is possible.

1.3.5 Non cooperative rendezvous

Considering two spacecrafts on different orbits, the main difficulties met by engineers and astronauts while wondering about rendezvous at the beginning was the full understanding of the relative motion of the two spacecrafts. Speaking about Apollo programme, André Meyer, already a Gemini Project engineer, explained the first unsuccessful attempt in rendezvous performed by Gemini 4 [19]:

There is a good explanation for what went wrong with rendezvous. The crew, like everyone else at MSC [Manned Spacecraft Center], just didn't understand or reason out the orbital mechanics involved. As a result, we all got a whole lot smarter and really perfected rendezvous maneuvers, which Apollo now uses.

The first rendezvous took place in the sixties. After the Russian attempt with its first manned programme Vostok, NASA's spacecrafts Gemini 6 and Gemini 7 managed in performing a rendezvous and station keeping, without getting in touch, in December 1965. Since then, rendezvous have been successfully performed to carry crews and supplies in an orbiting space station (as it happened for the first time with Salyut 1 in 1971, and then with Skylab and Mir). When it became possible, manned operations have been aided and, in last decades, also replaced with autonomous robotic rendezvous, as it currently happens for most of the ISS dockings.

From that 1965 giant improvements have been made in the knowledge of orbital relative dynamics and in robotic technology. Satellites constellations are becoming widely used for any kind of purpose and autonomous formation flying it is more and more a requirement. So far, the common denominator is the active role of the players. Although in a rendezvous, manned or unmanned, there is usually an active spacecraft, the chaser, e.g. the Soyuz carrying a crew to the ISS, and a passive one, the target, e.g. the ISS waiting for the Soyuz to approach, both spacecrafts can communicate each other and everything about absolute position and velocity and both attitudes are known. This is the main feature of a cooperative rendezvous.

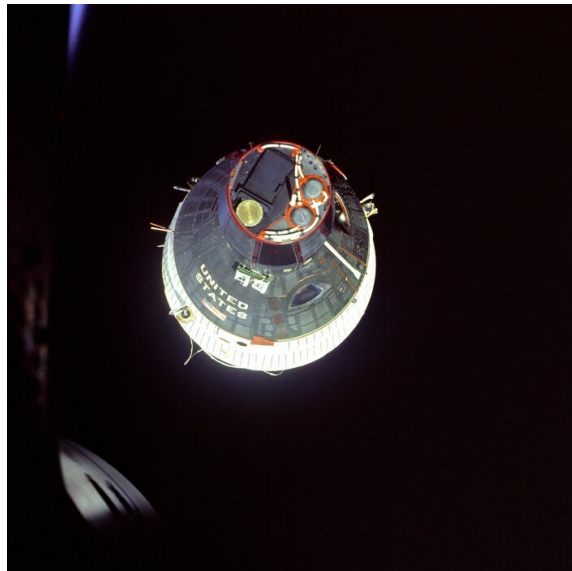


Figure 1.9: Gemini 7 spacecraft seen from Gemini 6 during their rendezvous, December 1965 (credits NASA)



Figure 1.10: Astronauts of STS-49 handling Intelsat 603 satellite (credits NASA)

approaching a non-cooperative object, please refer to some Space Transportation System (STS) missions, where crews of the Space Shuttle sometimes had to face the recovering of a satellite, launched during some previous missions and for this already in orbit (a manned non-cooperative rendezvous indeed). As an example, on May 1992 the crew of STS-49 mission [20] – first flight of the Space Shuttle Endeavour – recovered a telecommunication satellite that was stucked in the wrong orbit since it had failed the perigee kick. Three astronauts grabbed with hands the 4.5 tons satellite and fixed it to the cargo bay (Figure 1.10). This kind of episode is remarkable since it gives the idea of what happens when a average person slowly touches an object heavier than a car in space: little contacts could lead the object to drift or spin in undesirable manners. Indeed, in those cases where the satellite to be recovered costs several millions of dollars (in this case was 150M dollars), NASA preferred to use astronauts in Extra Vehicular Activities rather than only the robotic arm, although far more dangerous for the astronauts, these were more reliable.

Laying in this aspect is the major challenge of performing a rendezvous with a non-cooperative object. Rendezvous always concern two cooperative players: they can cooperate by sharing information, performing maneuvers, phase their relative attitude. If one of them is not cooperative, the other is required to balance. In the last ten years many efforts have been made in order to fully understand how to perform rendezvous and station keeping among two spacecraft without any crew and, more recently, the problem of non-cooperative rendezvous rose up. The state of the art will be examined in depth in Chapter 2.

To understand the difficulties in ap-

1.4 State of the art

Non-cooperative rendezvous firstly recalls the topic of formation flying. Formation flight has been more and more developed in recent years mainly with respect to scientific in-orbit experiments requiring an extremely precise positioning of two or more spacecrafts. It is commonly identified as the collective usage of two or more cooperative spacecraft to exercise the function of a single monolithic virtual instrument. Such an aim can be achieved only if the spacecrafts work together autonomously. Autonomous formation flight is a technical challenge of great interest for many scientific missions. Among other applications the design of synthetic apertures is a promising benefit of using distributed spacecraft. As an example, higher angular resolution in astronomical images requires increasing apertures of telescopes or increasing baselines of interferometers. The mass of the support structure of the telescopes increases accordingly, and propellant for launch and navigation of long baseline space telescopes may easily exceed technical and financial boundaries. The idea of formation flying allows to overcome the mass constraint combining satellites in autonomous formation flight to behave just like a rigid body. Missions like SWARN, PROBA 3 and all the successive ones born after this [21].

In an ADR mission, the first approach to think about is the “leader-follower” formation. A more detailed discussion will be done in Chapter 2, about the assignment of such labels to chaser and to target. In leader-follower coordination approach, one leader spacecraft is controlled to a reference orbit, and the other follower spacecrafts in the formation control their relative state to that leader. This approach allows traditional periodic maneuvers to keep the leader in a desired orbit or ground-track, while the remaining satellites in the formation control their relative state with respect to the leader.

The present study has been carried on starting from some recent missions and experiments.

1.4.1 PRISMA

Launched on June 15, 2010, Prototype Research Instruments and Space Mission technology Advancement (PRISMA) mission played as a demonstrator of autonomous formation flight and rendezvous technologies [22]. It consisted of two spacecrafts, Mango and Tango, launched together in a Sun synchronous orbit and then separated each other: Mango was then performing observations of Tango and maneuvering to modify the formation. The two satellites spaced a relative distance from about 1 m to 45 km, as shown in Figure 1.11. The mission qualified a series of sensor and actuator systems including navigation using GPS, Vision Based and RF technology as well as a propulsion system based on environmentally friendly propellant technology. The mission also included a series of GNC experiments using this equipment

in closed loop.

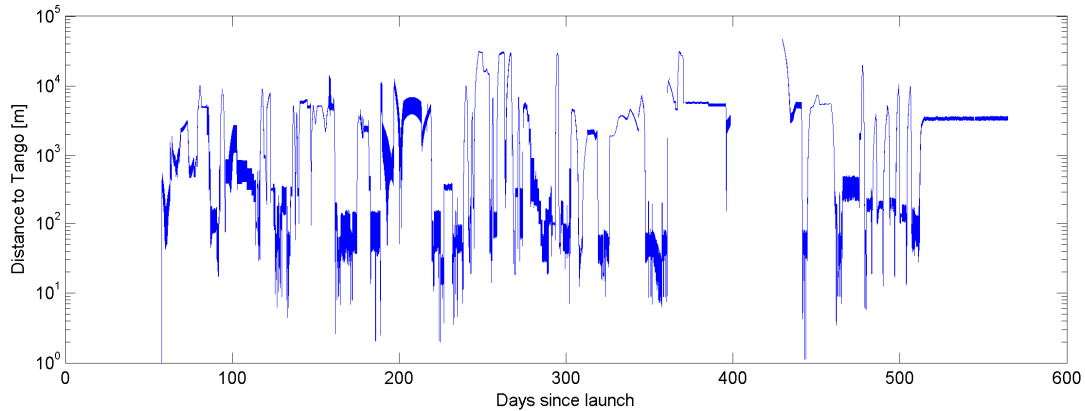


Figure 1.11: GPS-based relative distance between Mango and Tango over time, up to December 31, 2011.

PRISMA has demonstrated a large variety of aspects of formation flying and rendezvous. The GNC experiments include several sets of experiments involving closed loop orbit control. It was a milestone as it demonstrated both the suitability of GPS-based navigation in LEO and the capability of autonomous vision-based navigation and rendezvous [23][24].

1.4.2 TanDEM-X

TanDEM-X is the name given to TerraSAR-X's twin satellite and the name given to the coupled flight mission. The couple of spacecrafts of the Earth observation mission TerraSAR-X was launched on June 21, 2010. The two satellites were meant to fly in a closed controlled formation, with distance of about 200m and 500m, scanning region of the Earth below with a Synthetic Aperture Radar. A starting point of this study has been the TanDEM-X Autonomous Formation Flying (TAFF) system, implemented in the mission, with particular attention to the design of the guidance, navigation and control system enabling the autonomous relative control of two spacecraft flying on near circular orbits [25]. The validation of TAFF showed that control performance at the meter level could be achieved, and the in-flight operations confirmed this expectation. The two spacecrafts remained in their sun-synchronous dawn-dusk orbit with a mean altitude of 515 km, inclination of 97.44 deg and nominal revisit period of 11 days (i.e. the nominal period of rearrangement of the formation). For setting up the effective baseline, TanDEM-X was separated from TerraSAR-X in the right ascension of the ascending node [26]. This spanned a horizontal baseline, which was adjusted between 200 m and 3000 m to achieve the effective baselines required for acquisition at different latitudes. An additional vertical separation at the northern and southern turns was achieved by a relative

shift of the eccentricity vectors of the satellites. The result is a complete separation of the two satellite orbits called Helix-formation, which enables a safe operation of close formations with minimum collision risk.

1.4.3 AVANTI

The Autonomous Vision Approach Navigation and Target Identification (AVANTI) experiment, successfully conducted in November 2016 by the German Aerospace Center (DLR), realized the first fully autonomous close approach of an unmanned spacecraft to a noncooperative target object in LEO. The main peculiarity of this demonstration is the low-cost minimalistic design strategy that had been adopted for the chasing spacecraft, since the onboard star-tracker had been used as a far range camera to take images of sky. This was the only real-time source of observations. The AVANTI spaceborne GNC system carried out autonomously the following activities [27]:

- image processing and target identification to extract the angle-measurements of the line-of-sight (LOS) to the target;
- real-time relative navigation;
- computation of the impulsive maneuvers' profile required to perform a rendezvous in a safe, fuel efficient manner.

The spaceborne algorithms, constituting the core of the experiment, have been embedded as passenger software on BIROS, a German Earth observation satellite launched in June 2016 as part of the FireBird constellation. This choice was motivated by the fact that this spacecraft was carrying a third-party picosatellite (BEESAT-4) to be released in orbit using a dedicated ejection mechanism, which means that an appealing target was already available to support the experiment without the need of spending propellant to rendezvous with an existing object. In addition, BIROS could grant access to the key hardware devices required by the experiment: a camera and a propulsion system. No additional formation-flying sensors or actuators were used. Therefore, the entire experiment has been designed to use one of the star cameras as unique sensor to track the target object. AVANTI has been developed relying on the experience already collected in 2012 using the PRISMA formation flying testbed, which performed angles-only relative navigation activities. [28]

In this sense, AVANTI pursued a low-cost approach, and no further formation-flying specific sensors and actuators have been embarked on the already designed BIROS satellite. Both orbit and platform characteristics of BIROS posed several challenges to develop an autonomous, spaceborne, vision based GNC system. Nevertheless, on the one hand these challenges embody ordinary requirements for realizing a realistic and general on-orbit servicing mission. On the other hand, AVANTI could

demonstrate the viability of the AO approach in a kind of worst-case situation. As a result, compared to the AO in-flight activities that DLR and other companies and institutions carried out on PRISMA, AVANTI had to advance both guidance and navigation solutions proposed so far. The implemented guidance policy tackles a deltaV minimum problem to reach a target relative state at a given time which supports the definition of user-defined time constraints and produces a solution continuously compliant with the passive-safety criterion, as explained later. This last feature, in fact, is a crucial aspect for a truly non-cooperative scenario, leading to the generation of spiralling rendezvous trajectories. The navigation system, on the other hand, implemented advanced algorithms to robustly identify the target despite the frequent observation outages. Moreover, it encompasses the estimation of the mean time-derivative of the relative semi-major axis, to catch the strong effect of differential non-conservative orbital perturbations [29]. The distance between the satellites is affected by a sinusoidal-like pattern. This is since, for safety reasons, the approach has been executed in a spiralling fashion. This peculiar relative motion is the consequence of the adopted passive formation safety concept. In Figure 1.12 the achievement of the main objective of the AVANTI experiment can be observed, i.e. the demonstration of far-to-mid range autonomous rendezvous capability.

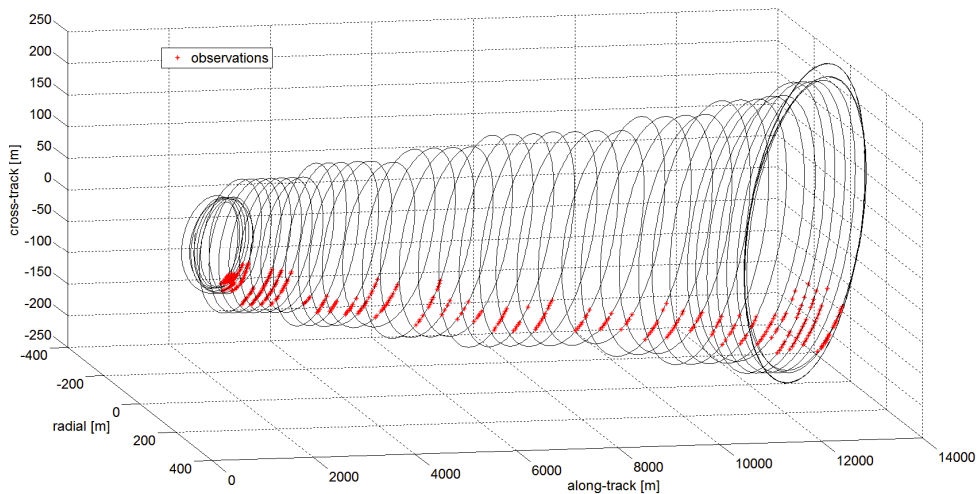


Figure 1.12: Spiral relative trajectory

It is important to note that the target needed to be in the visibility range of the chaser, and that its orbit was coarsely known thanks to the knowledge of TLE data.

AVANTI demonstrated the affordability of AON approach to perform far- to mid-range navigation, in order to bring the chaser satellite at a separation distance where close-proximity specific sensors may be used. At close range, camera starts to be affected to centroid errors, due to the reflection of the light by target surfaces, that give biased information about the center of mass of the target. Through Figure

1.13, the entity of such biased observations can be appreciated.

Moreover, BIROS could only rely on a star-tracker, which is a far-range camera, and the onboard computer could not process enough pictures in a time interval needed for close-range operations (the maximum data rate was one picture each 30 seconds). For these reasons, AVANTI accomplished the task of the far- to mid-range experiment (which actually constituted the primary goal of the demonstration) but, at close-range, more robust guidance is required [30].

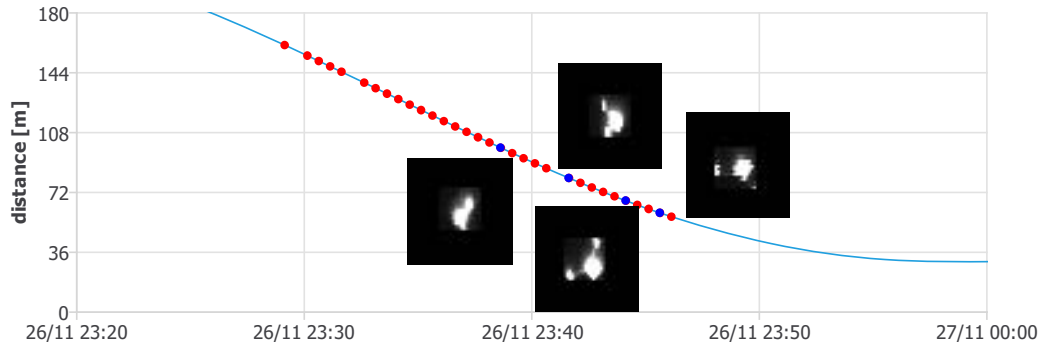


Figure 1.13: Measurements during the close-range approach

Blue dots correspond to the time when the four images have been acquired. As long as the target is far, illuminated areas may be considered almost coincident with the center of mass. At close-range, size and shape of the target make the centroiding computation harder [30].

1.4.4 CleanSpace One

Even if this project has not seen the light yet, it is worthy of mention as it is one of the main backgrounds of ClearSpace-1 mission. Since 2010, researchers at EPFL's Space Center (eSpace) have been at work on new space debris rendezvous-and-capture systems as part of the CleanSpace One project. The motivation behind the CleanSpace One project was to advance Technology Readiness Levels (TRLs) and start mitigating the impact on the space environment by acting responsibly and removing "debris" from orbit. The objectives of the CleanSpace One project were mainly to increase awareness regarding space debris, demonstrate ADR technologies and de-orbit a SwissCube.

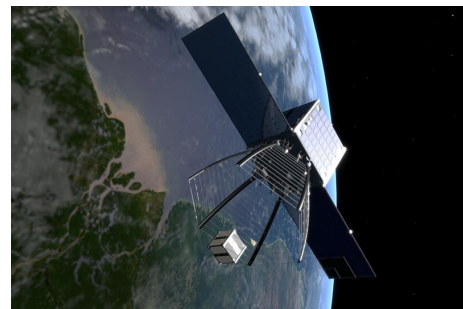


Figure 1.14: Artistic illustration of the "Pac-Man" configuration for CleanSpace spacecraft (credits EPFL)

SwissCube is the first Swiss-owned and student-designed satellite. It was launched on September 23, 2009 and has been operational since and all subsystems of the satellite are still performing nominally. SwissCube is a 1-Unit CubeSat (100 x 100 x 113.5 mm³), and it weighs 820 g. It is on a Sun synchronous orbit at about 720 km altitude and 98.4 deg inclination. The original configuration of the chaser considered a deployable net as capture system, capable of including the small target inside a closed volume, as shown in Figure 1.14. CleanSpace One project was officially initiated in 2012 and kept on advancing and improving its knowledge, until it represented the starting point for ClearSpace startup in 2018.

Concluding this overview, a remarkable point lies in the possibility of “communication” with the target. In PRISMA, even if a completely non-cooperative rendezvous was simulating, Mango could rely on some information known directly from the target Tango itself and they were able to share each other GPS signals. Indeed, PRISMA’s primary objective was to test autonomous formation flying. The next step came with AVANTI. This time the two spacecrafts couldn’t communicate with each other. Therefore, BIROS could only rely on vision-based navigation capability and the a priori known information about BEETSAT-4 was only the TLE: this aspect is the same for an ADR mission, since the target position and velocity can be known by mean of TLE data or direct ground observations. Such information is needed in order to reach the same orbit but is not enough to perform a closing or a rendezvous. AVANTI developed a GNC system completely based on AO navigation and moved from ground-based approach to fully autonomous onboard operations. Moreover, the experiment highlighted the limitations of AO applicability to the close-range domain: a vision-based only navigation system can not assure the same results in mid- to close-range navigation and formation keeping as performed in far- to mid-range.

1.5 ClearSpace

At the Space19+ Ministerial meeting in Seville, Spain, in late November 2019, the 22 European Space Agency member states committed a budget to fund ESA programs over the following three years. The budget finances every project promoted by ESA, from Earth Observations to Telecommunications, from Space Transportation to Human and Robotic Exploration, and many others, including Space Safety. Concerning the latter, the European Space Agency (ESA) has selected a startup to lead a consortium and execute a landmark Active Debris Removal (ADR) mission under the recently introduced Space Safety Programme. EPFL spin-off ClearSpace will head the ADRIOS activity, developing technologies to cap-

ture and de-orbit space debris. The ClearSpace-1 mission will involve recovering a VEGA Secondary Payload Adapter (VESPA) Upper Part, the first adapter successfully used of its kind, flown in 2013 during the second flight of VEGA. It is a cone-shape object with a diameter of 2 m, a height of 1.8 m and 120 kg of mass.

The ClearSpace-led consortium was selected out of 13 European and Canadian consortia. Eight ESA member states have pledged funding for the ClearSpace-1 mission and will together contribute to the ADRIOS programme.

ClearSpace-1 will be the first space mission to remove an item of debris from orbit, planned for launch in 2025. The mission aims to help establish a new market for in-orbit servicing, as well as debris removal. ClearSpace was born from the EPFL's Space Center (eSpace), that has been working since 2010 on new space debris rendezvous-and-capture systems as part of the CleanSpace

One Project, which aimed to develop and build the first satellite family designed explicitly for space debris cleaning. In early 2018, the startup was founded to pick up where the project left off – and turn the idea into a viable, sustainable business model.

The startup's first debris-clearing space robot was indeed designed to de-orbit Swiss-Cube, a Cubesat-type nanosatellite launched into orbit by EPFL and its partners in 2009. The company will now repurpose its space robot to capture the VESPA adapter. The “chaser” space probe will be launched into the target orbit where it will track down VESPA, grab it using a quartet of robotic arms and drag it out of orbit, with VESPA and the chaser both burning up in the atmosphere on the way down to Earth. A future ambition is to create a clear-up robot that could eject junk into the atmosphere, before continuing to capture and de-orbit other pieces of junk.

1.5.1 VESPA adapter

As mentioned previously, ESA pointed out debris to be removed first as those with high mass. Fragmentation and collisions generate debris clouds. The more significant is the involved mass, the greater or the more are the generated debris. A passive body with a great mass is a potential source for many other debris. In its Space Environment Report [1] ESA focuses on the amount of debris in space, classifying per type of orbit. The debris population is classified mainly according to three



Figure 1.15: ClearSpace logo

parameters: mass, area and object count. In order to give priority to the targets to be removed, the most critical parameter is mass. (This led ESA to point out a list of objects in LEO). The VESPA adapter is not one of the most relevant objects by mass, with its mass of barely 120 kg. Nevertheless, it is a good compromise between mass, dimensions and simple geometry and shape and sturdy construction. ClearSpace-1 mission will be the first Active Debris Removal mission ever done. For this reason, its landmark and demonstrative feature is very important and consequently its prescribed target must be representative but simple in being captured.



Figure 1.16: VEGA payload bay and one fairing.

VESPA is composed of two composite structures. The designated target for ClearSpace-1 mission is the conical shape upper part [31]

This type of adapter has been thought for a payload mainly composed by mini satellites. In a multiple launch configuration, the VESPA allows to embark several passengers inside the fairing. This payload configuration, consisting in two main adapters, makes VEGA able to carry a primary payload of 1000 kg on top of the VESPA and a secondary payload of 600 kg below it, inside the adapter's vain. The VESPA consists of a load bearing carbon structure, comprising a cylindrical part enclosing the lower passenger(s) with their adapter, and an upper conical shell supporting the main passenger [31]. In its second flight in 2013, VEGA delivered three satellites in Sun-Synchronous Orbit. The separation of the last satellite from the fourth stage happened at about 665 km of altitude and at 98.1° of inclination. Since then, whereas perturbations have occurred, the fourth stage and the adapters have kept on orbiting in a polar orbit with these features. Considering the TLE format, constantly provided by NORAD, the

orbit of the fourth stage is known. The fourth stage hosted the AVUM, the last propulsion module of the launcher, and the adapter. The last separation occurred six minutes after the separation of VESPA from the fourth stage. By knowing the current orbit of the AVUM stage, one can assume with enough confidence that

VESPA is on a very close orbit. As an example, a recent (as regards the time the author is writing) single AVUM's TLE is reported:

```
1 39162U 13021D 20025.60863441 .00000107 00000-0 41010-4 0 9997
2 39162 98.8483 231.9943 0094685 241.3967 117.7674 14.48125288354961
```

Without caring about each information reported by the TLE data format, here the main ones:

Data from TLE				
epoch	year	day of the year	fractional day	date
	20	025	0.6086441	25th Jan 2020, 14:36:26 UTC
orbit	inclination [deg]	eccentricity	mean motion [rev/day]	semimajor axis [km]
	98.8483	0.0094685	14.48125288	7109.9
				altitude [km]
				738

Table 1.1: Some of VESPA's orbital parameters at a given epoch.

Last column of Table 1.1 reports derived information, as the date of the epoch and the semi-major axis. The latter has been computed from the mean motion, since the latter is

$$n = \sqrt{\frac{\mu}{a^3}} \quad (1.1)$$

having considered the equality $1 \frac{rev}{day} = \frac{2\pi}{86400} \frac{rad}{s}$.

The altitude h represents an average, derived from the semimajor axis a and the mean Earth Radius R_e , as

$$h = a - R_e$$

It is essential to underline that VESPA's orbit itself can be determined from TLE data and ground observations, as pointed out in Section 1.3. This kind of information could be theoretically enough to approach the object in its own orbit with errors of the magnitude of tens of meters. Then the final approach – which the present study is interested in – must be performed autonomously by the chaser. Table 1.1 precisely recalls the initial situation of the present study: the orbit of VESPA is known, the chaser has already performed phasing and is about to begin approaching from far-range to mid- and close-range.

Chapter 2

Fundamentals

This chapter deals with the theoretical basis of the present study. In order to control the formation, the chaser must accomplish two tasks mainly: to derive the current state of the formation and to decide the manoeuvres to perform. These two tasks are what one can recognise in a classical feedback control law. On-board sensors take measurement of the real state - i.e. current relative position of the target with respect to the chaser – and an observer should be able to derive the current state thanks to these measurements and to a dynamical model, which approximates the state transition in time. Then, when required, the chaser must decide the magnitude of the manoeuvres in order to maintain the desired nominal formation, or to reconfigure it. As the observer, the controller relies on the simplified dynamical model too.

First, a brief recall about orbit dynamics is made with the assumption that both the chaser and the target lie on near-circular LEOs. The intent is to present a simple dynamical model which has been implemented in the GNC system. This model needs to consider the environment of Low Earth Orbit in order to predict the relative motion between target and chaser and to decide the magnitude of manoeuvres. Then, a control strategy is needed. The main aim of this study is to investigate mid- to close-range relative navigation and formation keeping at close-range. In order to maintain a formation, periodic checks and manoeuvres are required, so a control strategy must be deployed. A simple control algorithm is presented, having considered impulsive manoeuvres. The chaser is provided with a propulsion system equipped with hydrazine thrusters and the aim is to ensure the feasibility of the close-range navigation for a prolonged time interval.

Finally, the adopted estimation technique is described. In order to keep a nominal formation, the on-board system needs to estimate the state of the dynamical system, i.e. current relative position and velocity vectors. The control strategy must be supported by a state observer. As described further, the dynamical model's non-linearities drove the choice towards the Extended Kalman Filter (EKF) architecture. For the need of the on-board GNC system, Kalman filtering is a very suitable real time estimation solution.

2.1 Orbital dynamics

Starting point is the well-known two body problem [32]. Given a central body -e.g. the Earth- and a second body -a spacecraft- and by assuming:

- spacecraft's mass, m_j , negligible if compared to the Earth's one, m_\oplus ,
- perfect spherical shape of the Earth, with radius R_\oplus , so the mass can be assumed to be concentrated in its center,
- no external nor internal forces acting on the system composed by the two bodies other than gravitational forces, acting along the line joining the center of the two bodies.

The equation of motion in an inertial reference frame, is the familiar vector differential equation

$$\ddot{\mathbf{r}} = -\frac{\mu}{r^3} \mathbf{r} \quad (2.1)$$

Where $\mu = G(m_j + m_\oplus) \approx Gm_\oplus$ is the motion gravitational parameter, approximated with the primary body's gravitational parameter since for the Earth and a 100 kg spacecraft the mass ratio is about $m_\oplus/m_j \approx 10^{22}$.

The equation describes the evolution of the secondary body position $\tilde{\mathbf{r}}$ expressed in absolute frame with respect to the primary one. The solution of the differential equation describes the geometry of a conic on its plane, i.e. the orbital or perifocal plane. On the perifocal plane, the radius pointing the spacecraft from the Earth's center is expressed as:

$$\mathbf{r} = \frac{p}{1 + e \cos \nu} \quad (2.2)$$

Where p is the semilatus rectum of the conic, e its eccentricity and ν the true anomaly, which is the angular position of the spacecraft in its orbit, as will be explained later.

The absolute state of the spacecraft, i.e. the position and velocity vectors in an inertial frame, needs to be known in order to characterise an orbit. The inertial frame adopted in this study is the usual Earth Centered Inertial (ECI), in particular J2000, whose x-axis points the vernal equinox, z-axis coincides with the direction of Earth rotational velocity and y-axis completes the right-hand frame. The XY-plane lays on the equatorial plane, so it is consequently tilt with respect to the ecliptic plane by an angle equal to the inclination of Earth axis. Figure 2.1 illustrates the inertial frame.

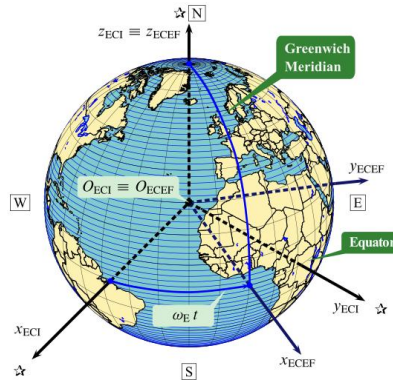


Figure 2.1: ECI and ECEF frames

ECI frame is shown together with the ECEF frame to underline the aspect of non rotation of the first, while the equatorial plane of the latter is co-moving with Earth rotation

Position and velocity are both 3D vectors, for an overall set of the state vector y_{ECI} of 6 components:

$$y_{ECI} = \begin{bmatrix} \mathbf{r}_{ECI} \\ \mathbf{v}_{ECI} \end{bmatrix} = \begin{bmatrix} r_X \\ r_Y \\ r_Z \\ v_X \\ v_Y \\ v_Z \end{bmatrix} \quad (2.3)$$

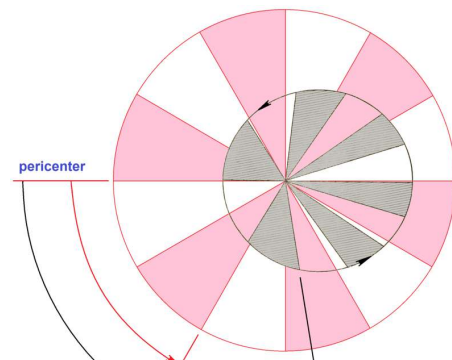
Six independent parameters also describe the geometry of a Keplerian orbit. Indeed, Keplerian Orbital Elements (KOE) are another way to describe the motion in the inertial frame and a biunivocal relation among KOE and absolute state exists [32].

In this study, mean anomaly is preferred to true anomaly. Mean anomaly is defined within the Kepler's equation, Eq. 2.4, to solve the problem of time dependency of the motion [32].

$$M = nt_P = E - e \sin E \quad (2.4)$$

Where n is the mean motion of the orbit, as defined in 1.1, t_P is the elapsed time since the last passage through the perigee. the eccentric anomaly, E , is related to the true anomaly by $\cos E = \frac{e + \cos \nu}{1 + e \cos \nu}$.

Mean anomaly averages the orbital motion and varies constantly in time. Instead of specifying the time of perigee passage to describe the orbit, it is customary to intro-



duce the value M_0 of the mean anomaly at some reference epoch t_0 . It follows that, at any arbitrary time t , the corresponding mean anomaly M is defined as

$$M = M_0 + n(t - t_0)$$

Mean argument of latitude $u = \omega + M$ is the angle travelled by the spacecraft from the ascending node to the current mean anomaly and can be used instead of mean anomaly in order to help avoiding singularities. Many other orbital elements sets have been proposed through decades so far, equivalent to classical orbital elements, mainly due to singularities that may occur for some values as summarised in Table 2.1 [33].

Keplerian Orbital Elements		singularities	
a	semi-major axis		
e	eccentricity	$e = 0$	
i	inclination	$i = 0^\circ$	$i = 180^\circ$
Ω	right ascension of the ascending node		
ω	argument of perigee		
ν	true anomaly		

Table 2.1: Keplerian Orbital Elements and singularities

The eccentricity vector belongs to the periapsis direction, pointing outward from the center of the primary body to the location of perigee on the orbit. This vector can be decomposed in two components, laying on the line of nodes and on the perpendicular direction belonging to the orbital plane, so that the angle used is the argument of perigee ω (see later Figure 2.5 to understand usefulness of this nomenclature).

$$\mathbf{e} = e \begin{bmatrix} \cos \omega \\ \sin \omega \end{bmatrix} \quad (2.5)$$

The present study considers a non-singular Keplerian orbital elements [34] and the elements vector is then written in a form that will be used so on, as depicted in

Eq. 2.6.

$$\alpha = \begin{bmatrix} a \\ u \\ e_x \\ e_y \\ i \\ \Omega \end{bmatrix} \quad (2.6)$$

2.1.1 Unperturbed relative motion

Two spacecrafts in orbit around Earth follow their own equations of motion, described by Eq. 2.1 for simple Keplerian motion. As reported in 1.3.5, topics such as rendezvous had faced the problem of understanding the behaviour of a spacecraft in its orbit with respect to a close spacecraft in another orbit. For circular orbits, the equation of relative motion is provided by Hill's equation, derived in the lunar theory [35]. The system of three linear differential equations is written in Radial-Transverse-Normal (RTN) frame – also known as “*Hill's frame*” or Local Vertical Local Horizontal (LVLH), where the coordinates (x, y, z) are computed on three local axis. The RTN frame is a useful spacecraft co-moving frame computed from the absolute position and velocity vectors.

$$\hat{\mathbf{o}}_{\mathbf{R}} = \frac{\mathbf{r}}{r} \quad (2.7)$$

$$\hat{\mathbf{o}}_{\mathbf{T}} = \hat{\mathbf{o}}_{\mathbf{N}} \times \hat{\mathbf{o}}_{\mathbf{R}} \quad (2.8)$$

$$\hat{\mathbf{o}}_{\mathbf{N}} = \frac{\mathbf{r} \times \mathbf{v}}{\|\mathbf{r} \times \mathbf{v}\|} \quad (2.9)$$

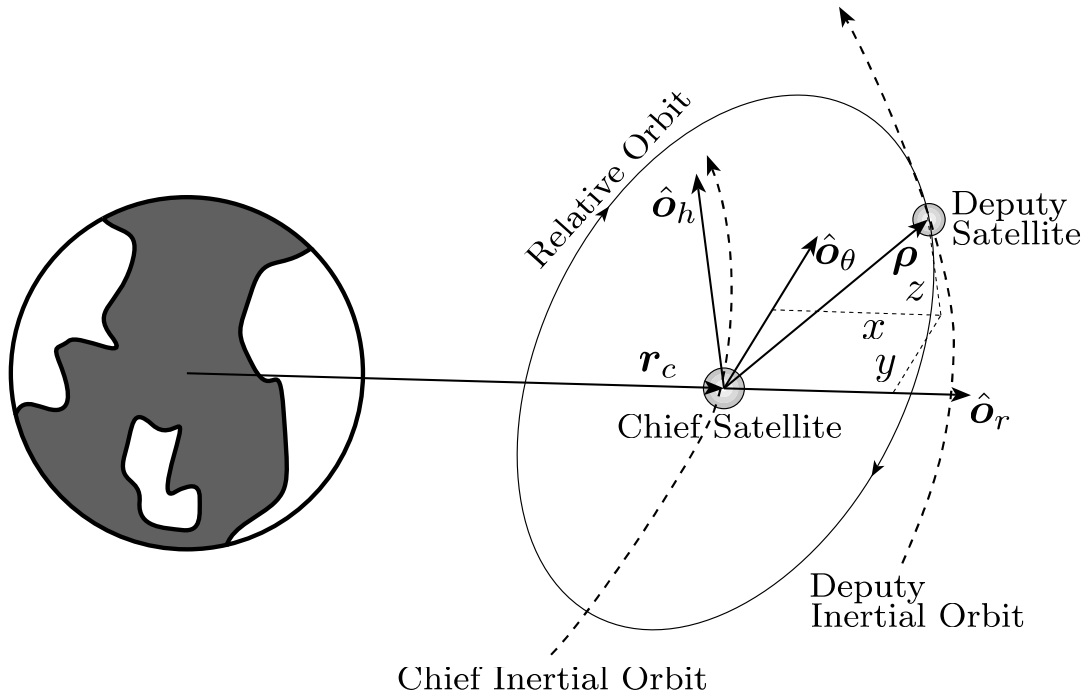


Figure 2.3: RTN frame, centered in chief satellite

Subscripts in image are not those used in Eq. 2.7. (r, θ, h) are shown instead of (R, T, N) and ρ represent the relative position vector, later pointed as $\delta \mathbf{r}$ [34].

One can see the right-handed frame in Figure 2.3 as:

- x on R axis (coincident with the position vector),
- y on N axis (coincident with the orbital angular momentum vector),
- z on T axis (completes the right-hand frame RTN, and the dot product with velocity vector is always positive).

Note: for a near circular orbit the unit vector along T direction is almost parallel to the velocity vector, $\hat{\mathbf{O}}_{\mathbf{T}} \parallel \mathbf{v}$.

The origin of the RTN frame is one of the two (or more) spacecrafts which motions are expected to be referred to a reference orbit. If only two objects are considered, these are labelled as:

- CHIEF, denoted by subscripts "d", the origin of the RTN frame,
- DEPUTY, the other spacecraft denoted by subscript "c", which motion can be independently moves in chief's RTN frame.

It follows that the relative state – i.e. relative position and relative velocity vectors– is the state of the deputy with respect to the chief.

$$\mathbf{y} = \begin{bmatrix} \delta \mathbf{r} \\ \delta \mathbf{v} \end{bmatrix} = \begin{bmatrix} \delta r_R \\ \delta r_T \\ \delta r_N \\ \delta v_R \\ \delta v_T \\ \delta v_N \end{bmatrix} = \begin{bmatrix} \Delta \mathbf{r} \cdot \mathbf{o}_R \\ \Delta \mathbf{r} \cdot \mathbf{o}_T \\ \Delta \mathbf{r} \cdot \mathbf{o}_N \\ \Delta \mathbf{v} \cdot \mathbf{o}_R + \Delta \mathbf{r} \cdot \dot{\mathbf{o}}_R \\ \Delta \mathbf{v} \cdot \mathbf{o}_T + \Delta \mathbf{r} \cdot \dot{\mathbf{o}}_T \\ \Delta \mathbf{v} \cdot \mathbf{o}_N + \Delta \mathbf{r} \cdot \dot{\mathbf{o}}_N \end{bmatrix} \quad (2.10)$$

where:

$$\Delta \mathbf{r} = \mathbf{r}_d - \mathbf{r}_c \quad (2.11)$$

$$\Delta \mathbf{v} = \Delta \dot{\mathbf{r}} = \mathbf{v}_d - \mathbf{v}_c \quad (2.12)$$

For distances between chief and deputy vehicles that are very small if compared with the orbital radii, a solution of the Hill linearized equations of relative motion has been derived from by W. H. Clohessy and R. S. Wiltshire in 1960 [36], under the assumptions of a **very short inter-satellites distance** and **almost circular orbits**:

- Very close orbits, i.e. $\Delta r \ll r_c$ and $\Delta r \ll r_d$,
- Near circular orbits, i.e. $e \ll 1$ so that the angular velocity is constant, $\frac{d\omega}{dt} = n$, mean motion.

It is noteworthy to stress these two assumptions, since lead to as many **approximations** that will constraint the model implemented by the GNC system. More attention to this concept will be given in Chapter 4. Hill's equations have been derived with such assumptions.

2.1.1.1 Hill's equations

Considering two spacecraft, a deputy and a chief of the formation, with two different orbits, the position of the deputy relative to the chief is

$$\mathbf{s} = \mathbf{r}_d - \mathbf{r}_c$$

and, by taking the second time derivative one can obtain for a pure Keplerian motion

$$\ddot{\mathbf{s}} = \ddot{\mathbf{r}}_d - \ddot{\mathbf{r}}_c \quad (2.13)$$

where \mathbf{f}_G represents the right-hand term of Eq. 2.1, function only of the absolute position vector and of the specific gravitational constant. If the two spacecrafts are closed enough, Eq. 2.13 can be linearised **-1st approximation-** around chief's

position. Deputy's function \mathbf{f}_G can be expanded up to the 1st order of a Taylor expansion as

$$\mathbf{f}_G(\mathbf{r}_d) = \mathbf{f}_G(\mathbf{r}_c) + \left. \frac{d\mathbf{f}_G}{d\mathbf{r}} \right|_{\mathbf{r}=\mathbf{r}_c} (\mathbf{r}_d - \mathbf{r}_c) + o(\mathbf{r}_d - \mathbf{r}_c) \quad (2.14)$$

where a higher order error as been introduced. The greater the inter-satellites separation s , the greater the error neglected. The approximation is then valid as long as $s \ll r$ roughly. The Jacobian $\frac{d\mathbf{f}_G}{d\mathbf{r}}$ can be derived and evaluated in $\mathbf{r} = \mathbf{r}_c$, as shown in [37], so that the equation 2.13 becomes linear in the variable \mathbf{s} . Eq. 2.15 shows the linearised Hill equations projected in chief's RTN coordinates [35].

$$\ddot{x} - \left(2\frac{\mu}{r^3} - \omega^2\right)x - \dot{\omega}y - 2\omega\dot{y} = 0 \quad (2.15)$$

$$\ddot{y} + \left(\frac{\mu}{r^3} - \omega^2\right)y + \dot{\omega}x + 2\omega\dot{x} = 0 \quad (2.16)$$

$$\ddot{z} + \frac{\mu}{r^3}z = 0 \quad (2.17)$$

If the orbits are almost circular, the angular velocity, i.e. the first time derivative of the true anomaly $\omega = \frac{dv}{dt}$, can be considered constant and here lies the **2nd approximation**. By setting $\dot{\omega} = 0$, Eqs. 2.15 can be analytically solved and lead to a closed form in which motions along x and y -i.e. radial direction and along-track direction- are coupled while motion along z-axis -cross-track direction- in independent and simple harmonic [36]. Eq. 2.18 reports the Clohessy-Wiltshire solutions, written in RTN frame.

$$x(t) = a_1 - a_3 \cos t - a_4 \sin t \quad (2.18)$$

$$y(t) = -\frac{3}{2}a_1 t + a_2 + 2a_3 \sin t - 2a_4 \cos t \quad (2.19)$$

$$z(t) = a_5 \sin t - a_6 \cos t \quad (2.20)$$

The solution in Eqs. 2.18 is only function of time, by mean of six integration constants a_j for $j = 1...6$ that depend on the initial condition. The integration constants have been read in literature in different ways, in order to get a mapping with Keplerian orbital elements for instance. The suitable expression of integration constants used in this study can be found in mapping from Keplerian orbital element differences to Cartesian Hill frame coordinates. By considering only the linearisation as approximation (and then considering arbitrary eccentricity), the relative position vector components are consequently given in terms of orbit elements in Eq.2.21 and well described in [38].

$$x(\nu) \approx \frac{r}{a} \Delta a + \frac{ae \sin \nu}{\eta} \Delta M - a \cos \nu \Delta e \quad (2.21)$$

$$y(\nu) \approx \frac{r}{\eta^3} (1 + e \cos \nu)^2 \Delta M + r \Delta \omega + \frac{r \sin \nu}{\eta^2} (2 + e \cos \nu) \Delta e + r \cos i \Delta \Omega \quad (2.22)$$

$$z(\nu) \approx r(\sin(\nu + \omega) \Delta i - \cos(\nu + \omega) \sin i \Delta \omega) \quad (2.23)$$

Where the $\Delta\alpha_j$ stands for the algebraic difference between deputy's and chief's orbital elements: $\Delta\alpha_j = \alpha_{jd} - \alpha_{jc}$. Dependency on time corresponds to the dependency on true anomaly. The mapping of 2.21 was made under the same hypothesis of Hill's equations, i.e. the linearisation around the position of the chief, and it is valid for any value of eccentricity (see $\eta = \sqrt{1 - e^2}$), as long as the two spacecraft are close enough.

2.1.1.2 Relative Orbital Elements

CW solutions in Eq. 2.18 can be write again thanks to their mapping in Hill orbital frame by mean of orbital elements differences as integration constants. Eccentricity is considered to be close to zero, enough to assume $\eta = 1$. This means that an upper boundary of about $e = 0.01$ shall be considered, as sketched in Figure 2.4. The limitation on the orbits' eccentricity has a great relevance and narrows down the set of orbits which can be modelled with CW solutions. Nevertheless, many objects in LEO lie on quite well circularized orbits, mainly because of perturbations, which will be treated in Section 2.1.2.

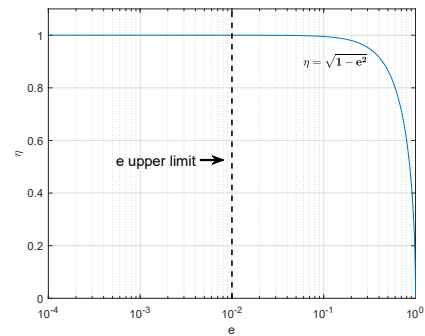


Figure 2.4: Eccentricity factor

Then, by introducing the assumption of near circular orbits and gathering Keplerian elements according to the formulation with eccentricity components and mean

anomaly, one can obtain [2]:

$$x(u) = \delta r_R = a\delta a - a\delta e_x \cos u - a\delta e_y \sin u \quad (2.24)$$

$$y(u) = \delta r_T = -\frac{3}{2}a\delta a u + a\delta\lambda + 2a\delta e_x \sin u - 2a\delta e_y \cos u \quad (2.25)$$

$$z(u) = \delta r_N = a\delta i_x \sin u - a\delta i_y \cos u \quad (2.26)$$

$$\dot{x}(u) = \delta v_R = na\delta e_x \sin u - na\delta e_y \cos u \quad (2.27)$$

$$\dot{y}(u) = \delta v_T = -\frac{3}{2}na\delta a + 2na\delta e_x \cos u + 2na\delta e_y \sin u \quad (2.28)$$

$$\dot{z}(u) = \delta v_N = na\delta i_x \cos u + na\delta i_y \sin u \quad (2.29)$$

Where RTN frame coordinates have been written as in 2.10

The orbital elements differences act as integration constants. Comparing Eq. 2.24 and Eq. 2.18 one can notice the similarity. Relative orbital elements then can be used as a suitable match of the integration constants of the CW solutions. This set is defined as Relative Orbital Elements (ROE) and gives the perception of geometrical relevance of those initial conditions [39]. Note that the decoupling between in-plane and cross-plane is still valid.

$$a\delta\alpha = a_c \begin{bmatrix} \frac{\Delta a}{a_c} \\ \Delta u + \Delta\Omega \cos i_c \\ \Delta e_x \\ \Delta e_y \\ \Delta i \\ \Delta\Omega \sin i_c \end{bmatrix} = \begin{bmatrix} a\delta a \\ a\delta\lambda \\ a\delta e_x \\ a\delta e_y \\ a\delta i_x \\ a\delta i_y \end{bmatrix} \quad (2.30)$$

ROE set is composed as follows: the relative semi-major axis $a\delta a = \Delta a$ is difference between deputy's and chief's semi-major axis and the relative mean longitude $\delta\lambda$ considers the along-track separation between the spacecrafts. Such parameterisation allows to consider the along-track separation not anymore on a straight line but as a circular arc of length $\delta\lambda$, having multiplied by the chief's semi-major axis. Relative eccentricity and relative inclination 2D vectors, $\delta\mathbf{e}$ and $\delta\mathbf{i}$, then give the size of the elliptical relative trajectory. Eq. 2.31 shows these two vectors both in cartesian and in polar components. Relative eccentricity vector can be seen in Figure 2.5, i.e. on chief's orbital plane. Note: relative eccentricity and relative inclination vectors do not lie on the same plane but such representation is useful to phase these vectors, as will be shown in Section 2.2. Relative eccentricity vector indeed lies on the chief's orbital plane while y-component of the relative inclination vector lies on the normal direction.

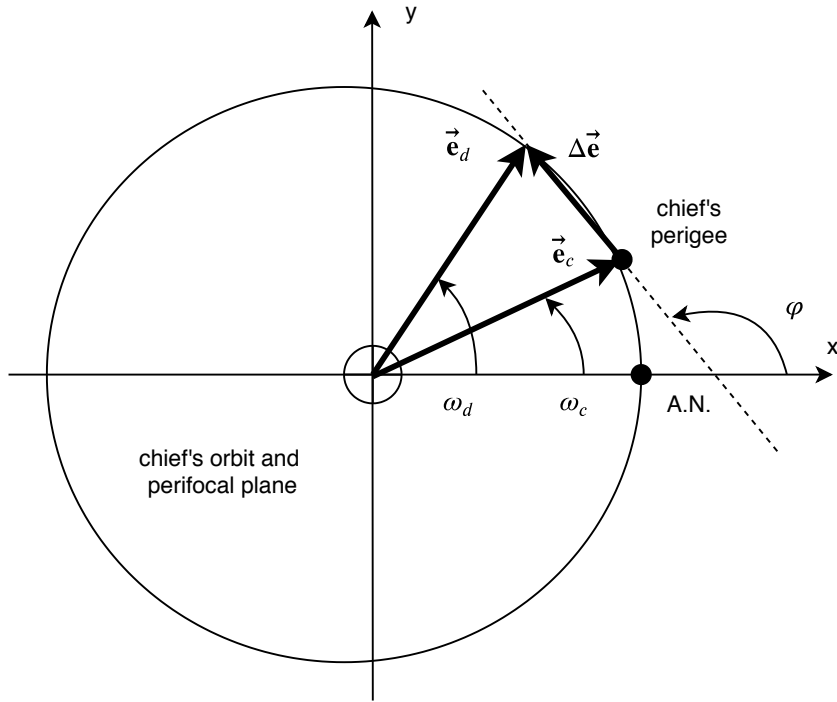


Figure 2.5: chief's and deputy's eccentricity vectors on chief's perifocal plane

$$\delta \mathbf{e} = \begin{bmatrix} \delta e_x \\ \delta e_y \end{bmatrix} = \delta e \begin{bmatrix} \cos \phi \\ \sin \phi \end{bmatrix} \quad (2.31)$$

$$\delta \mathbf{i} = \begin{bmatrix} \delta i_x \\ \delta i_y \end{bmatrix} = \delta i \begin{bmatrix} \cos \theta \\ \sin \theta \end{bmatrix} \quad (2.32)$$

ROE are then a way to describe relative motion considering the two approximations used in Section 2.1.1.1 and are directly related to the shape of the relative motion. A more accurate explanation of ROE derivation can be found in [39] and Figure 2.6 shows the projection of the relative trajectory on the chief's orbital plane (i.e. RT plane) and on the cross-track plane (i.e. RN plane), for a null relative semimajor axis. Indeed, since $a\delta\lambda$ increases linearly with time proportional to $a\delta a$, $a\delta a = 0$ assure a bounded relative motion.

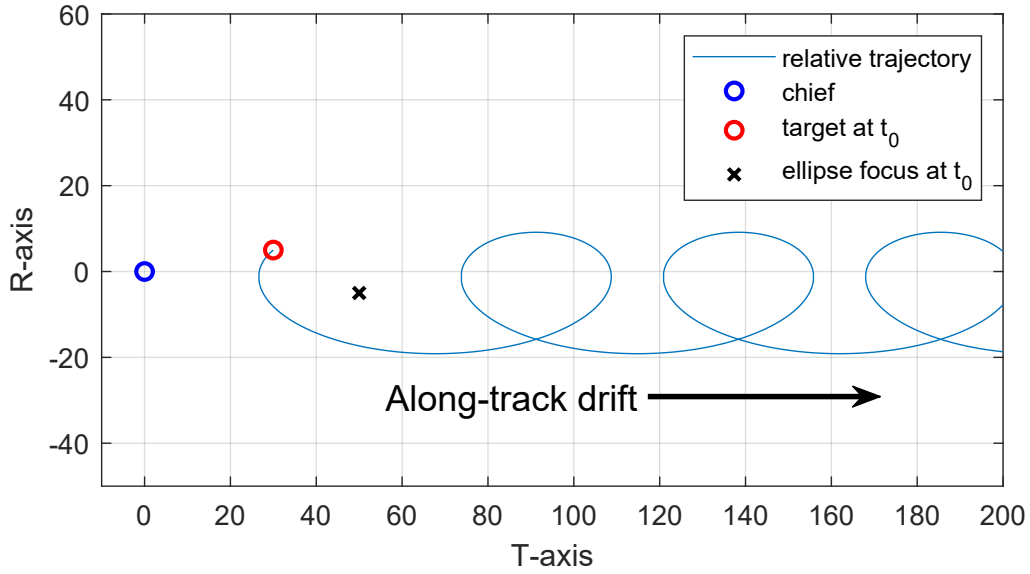


Figure 2.7: Along-track drift due to a non-zero relative semi-major axis

Relative trajectory on RT plane, computed according to Eq.2.24 with $a\delta\alpha = [-5, 50, -10, 10, 4, -10]$ m and a semi-major axis $a_c = 7000$ km

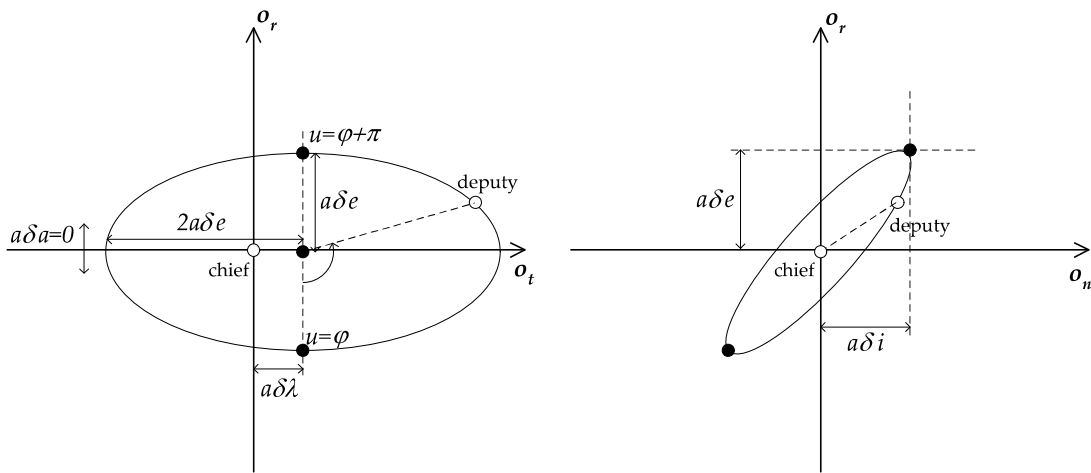


Figure 2.6: Relative trajectory projections on RT and RN planes [2]

If $a\delta\lambda = 0$ too, the formation is bounded and centered on the chief spacecraft. In general, for non-zero values of $a\delta a$ and $a\delta\lambda$, the formation is not centered at t_0 : in Figure 2.7 the center of the relative trajectory on RT plane has coordinates $a\delta\lambda \neq 0$ on T and $a\delta a \neq 0$ on R, in this case the formation is not bounded anymore, since a shifting occurs in along-track direction. A non-zero difference between semimajor

Geometric meaning of ROEs	
$a\delta a$	radial separation and along-track drift
$a\delta\lambda$	along-track separation
$a\delta\mathbf{e}$	major and minor axis on along-track (RT) plane
$a\delta\mathbf{i}$	separation on cross-track (RN) plane

Table 2.2: Geometric meaning of ROEs

axis leads indeed to a non-zero difference of mean motions and after one orbital period, i.e. 2π , the along-track separation accumulates to the amount of $3\pi\Delta a$. For a simple Keplerian motion, mean motion n is the time derivative of the mean argument of latitude u , $n = \frac{du}{dt}$. Difference in deputy's and chief's mean motions is considered in Eq. 2.33, with the assumption of very similar semi-major axis.

$$\Delta\dot{u} = n_d - n_c \approx -\frac{3}{2}n_c\delta a \quad (2.33)$$

$$(2.34)$$

since semi-major axis can be considered $\frac{a_d}{a_c} \approx 1$ even if $\delta a \neq 0$.

2.1.2 Perturbed relative motion

Once defined the relationship among relative orbital elements and relative state of the deputy spacecraft with respect to the chief, it is important to consider the perturbations experienced by the two spacecrafts. LEOs are widely affected by non-uniformity of the gravitational field, especially for what concerns Earth flattening, atmospheric drag and many others such as solar radiation pressure, third bodies, relativity etc [3]. These phenomena affect spacecraft motion such that it cannot be considered as simple Keplerian, since non-conservative accelerations are introduced. Even if far smaller in magnitude than the gravitational acceleration, such effects imply secular variations in orbital elements, determining a motion that is not pure Keplerian anymore. Typical acceleration magnitudes can be seen in Figure 2.8. In the presented model, deviation of the Earth gravity from spherical symmetry and dragging due to air layers -still present in the upper atmosphere up to about 2000 km altitude- are considered.

2.1.2.1 Gravitational field

For what concerns gravitational effects, only second order zonal coefficient is considered, J_2 . Zonal coefficients reflect the different Earth's mass distribution at different latitudes, because of the Earth's poles flattening. The first relevant zonal coefficient stands within the second order. Gravity potential U can be expanded from the perfect spherical Earth's shape form. First term in right-hand side of Eq. 2.35

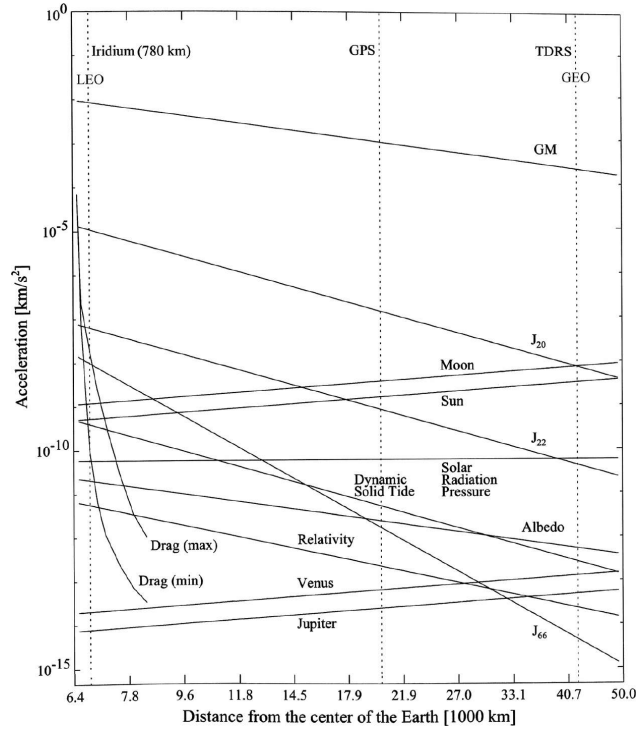


Figure 2.8: Perturbing accelerations in Earth orbits [3]

represents the perfect spherical Earth's shape.

$$\ddot{\mathbf{r}} = \nabla U \quad (2.35)$$

$$U = \frac{\mu}{r}(1 + \mathbf{f}_U(\mathbf{r})) \quad (2.36)$$

where \mathbf{f}_U is a function of the spacecraft absolute position vector and gathers all the higher order contributes, commonly used in literature in terms of spherical coordinates (radius, latitude, longitude) [3].

By neglecting all terms of order higher than 2 in Eq. 2.35, the gravitational potential of the Earth can be written as

$$U = \frac{\mu}{r} \left(1 - J_2 \left(\frac{R}{r} \right)^2 P_2(\sin \phi) \right)$$

where ϕ is the geographic latitude and P_2 the second order Legendre polynomial.

For Earth satellites with the altitudes between about 300 and 30000 km the effects of J_2 is the largest perturbation effect. Indeed, is $J_2 \approx 1.083 \times 10^{-3}$ while other coefficients are of the order of 10^{-6} . Since both deputy's and chaser's orbital elements vary in time due to J_2 effect, then the relative orbital elements will vary as well – as they are essentially defined as differences between deputy's and chaser's orbital elements. J_2 affects three orbital elements mainly: longitude of ascending node, argument of perigee and mean anomaly:

$$\dot{\omega}_{J_2} = \frac{3}{2} n \gamma (5 \cos^2 i - 1) \quad (2.37)$$

$$\dot{\Omega}_{J_2} = -3 n \gamma \cos i \quad (2.38)$$

$$\dot{M}_{J_2} = \frac{3}{2} n \gamma \eta (3 \cos^2 i - 1) \quad (2.39)$$

Assuming that these drift rates are the first order time derivative due to J_2 of these three orbital elements, by substituting the drift rates into the definition of ROEs one can obtain a transition law [2], that binds relative orbital elements at time t with the corresponding ones at time t_0 . Eq. 2.40 shows how the transition matrix only depends on the inclination of the chief orbit, the J_2 -perturbation and the elapsed time interval since t_0 .

$$\Phi(Du, \gamma, i) = \begin{bmatrix} 1 & 0 & 0 & 0 & 0 & 0 \\ -\frac{3}{2}Du & 1 & 0 & 0 & -\frac{21}{2}\gamma \sin(2i) Du & 0 \\ 0 & 0 & \cos(\varphi' Du) & -\sin(\varphi' Du) & 0 & 0 \\ 0 & 0 & -\sin(\varphi' Du) & \cos(\varphi' Du) & 0 & 0 \\ 0 & 0 & 0 & 0 & 1 & 0 \\ 0 & 0 & 0 & 0 & 3\gamma \sin^2 i Du & 1 \end{bmatrix} \quad (2.40)$$

$$Du = u(t) - u(t_0) \quad (2.41)$$

$$\frac{d\varphi}{dt} = \frac{d\varphi}{du} \frac{du}{dt} = \varphi' \frac{du}{dt} \quad (2.42)$$

$$\varphi' = \frac{3}{2}\gamma(5 \cos^2 i - 1) \quad (2.43)$$

$$\eta = \sqrt{1 - e^2} \quad (2.44)$$

$$\gamma = \frac{J_2}{2} \left(\frac{R_{\oplus}}{p} \right)^2 \quad (2.45)$$

where $i \equiv i_c$.

Note: here the notation u has been adopted only to avoid confusion with the algebraic operator, $\Delta(\cdot)$, used so far for differences between quantities of the deputy and the chaser. $D(\cdot)$ refers to the variation in time of the quantity, in this case the mean argument of latitude u of the chief, such that $Du = u(t) - u(t_0)$.

Note: to express variations of relative orbital elements as a state transition is useful in order to define a simple dynamical model to implement.

It is easy to visualize the behaviour of J_2 -affected relative orbital elements. The along-track separation is affected by all of the three drift rates in 2.37. Therefore, $\delta\lambda$, sees the contribution of J_2 drift added to the drift due to semi-major axis difference. Relative inclination senses J_2 drift only on one out of two components: the difference of inclinations does not vary, since the inclination itself is not affected by Earth oblateness, while the longitude of ascending node does, and this results in a linear drift in the relative inclination y-component. Finally, the relative eccentricity vector experiences a periodic variation due to J_2 . The $\delta\mathbf{e}$ vector rotates with a frequency that equals the perigee precession motion, since it is varying with the argument of perigee, omega. Figure 2.9 shows how relative inclination and relative eccentricity are affected by J_2 .

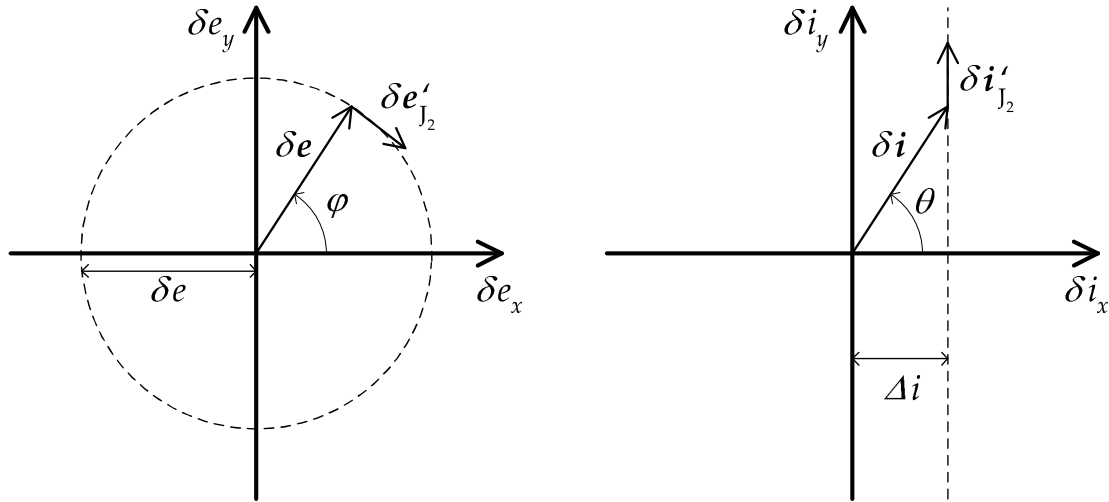


Figure 2.9: Relative eccentricity and relative inclination vectors variations [2]

2.1.2.2 Differential drag

Although the air in the upper atmosphere has very low density, it influences significantly the motion of satellites (the velocity of satellites amounts to about 10 km/s). Air drag can be understood as a result of friction between the air and the body of the satellite. As with all other friction forces the mechanical energy of the system does not remain constant but partially decreases, transformed into other sorts of energy. It means that a potential cannot be defined for the air drag force and should be considered using constant perturbation equations [32]. In general, modelling of atmospheric drag is a very complex problem. Here we consider the simplest case. More detailed discussion can be found e.g. in [?]. It is intuitive to consider the drag effect only within the orbital plane, since its effect slows down the spacecraft. Indeed, drag acceleration is antiparallel to the velocity, then no acceleration occurs on cross-track direction.

Each spacecraft experiences a drag acceleration opposite to its absolute velocity, as reported in Eq. 2.46. Moreover, under the assumption of near circular orbits, absolute velocity vector can be assumed to be parallel to the along-track direction, o_T .

$$\ddot{\mathbf{r}}_D = \frac{1}{2} \rho v^2 \frac{C_D A}{m} \frac{\dot{\mathbf{r}}}{\|\dot{\mathbf{r}}\|} \quad (2.46)$$

As the velocity decreases due to atmospheric drag, the spacecraft loses altitude. This loss results in a semi-major axis decrease. Therefore, both components of the in-plane motion are affected by drag acceleration. For a radial distance between the two spacecrafts up to about 10 km, density variations can be neglected [?]. The relative motion is then affected by differential drag only because of the different ballistic coefficient of each spacecraft, $B = \frac{C_D A}{m}$. The impact of differential drag

may be minimised by obtaining a minimum $\Delta B = B_d - B_c$. One can assume a constant angular deceleration due to the atmospheric drag, simply switching from a uniform angular mean motion to a uniformly decelerated motion. Assuming near circular orbits -i.e. almost equal semi-major axis and orbital velocities expressed as $v = an = \sqrt{\frac{\mu}{a}}$, the absolute acceleration experienced by one spacecraft along T-axis is then the product of the semi-major axis with the angular acceleration, and the radial variation can be assumed equal to the semi-major rate of change:

$$\frac{d^2 r_T}{dt^2} \approx a \frac{dn}{dt} \equiv -\frac{1}{2} \varrho v^2 B$$

$$\frac{dr_R}{dt} = \frac{da}{dt}$$

It follows that the formation experiences variations due to drag along R and T chief's axis. These are pointed out in Eq.2.47.

$$D(\delta r_T) = \frac{3}{4} \frac{v^2}{n^2} \varrho \Delta B Du^2 \quad (2.47)$$

$$D(\delta r_R) = -\frac{v^2}{n^2} \varrho \Delta B Du \quad (2.48)$$

Considering the target of the present study, VESPA, and that the chase will have approximately an equivalent mass – about 100 kg-, a differential ballistic coefficient $\delta B = \frac{\Delta B}{B}$ can be assumed in a range of (2%, 5%). According to the Jacchia model [?] [3] the atmospheric density at a representative altitude of 700 km lies in a range of about $(10^{-17}, 10^{-15})\text{g/cm}^3$, depending on solar flux conditions, as shown in Figure 2.10.

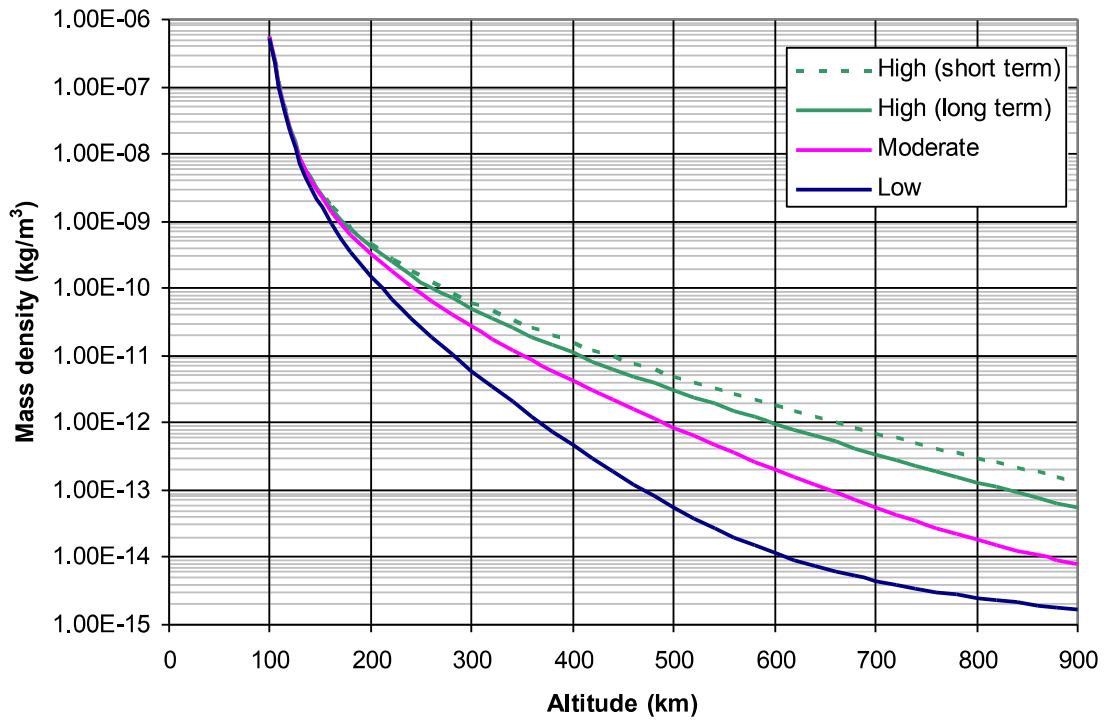


Figure 2.10: Atmospheric density

JB2008 mean air density with altitude for low, moderate, and high long- and short-term solar and geomagnetic activity (credits CIRA [40])

As described in [2] such conditions imply the necessity of velocity increments of magnitude from 1 mm/s to 5 mm/s to compensate the velocity drop collected in about 10 days. Even though these values might increase by a factor of 10 during high solar activities and geomagnetic storms, differential drag has evidently modest impact on the formation control during nominal operations even for LEO orbits, but can be relatively easily considered in the simplified dynamical model.

2.2 Relative state control

The presented dynamical model, already validated on PRISMA, TANDEM-X, AVANTI missions [30] [26] has its major contribution in simplicity. Therefore, is a useful resource to perform on-board computation. Recalling the importance of real time application, the numerical model has to be as simpler as possible. Present study is not intended to control the approach of the chaser to the target. This means that orbit injection and phasing are not considered. Formation reconfiguration and formation keeping are considered instead, that can be addressed as homing and closing: for instance, a scenario could see the chaser involved in passing from mid-range to close-range proximity, e.g. from 100m to 10m of relative distance, or also performing formation keeping for a long period of time.

As seen so far, relative state changes in time. Maneuvers are needed to restore the desired configuration of the formation deputy-chief. The objective of the present study is indeed to maintain a close-range formation for a certain time period, so it is convenient to refer the motion of the target to the chaser's reference orbit. Then, the formulation sees

- the CHASER as the CHIEF,
- the TARGET as the DEPUTY.

This choice do not affect validity anyway since whichever the spacecraft chosen as reference, the relative state does not vary its magnitude, but it is a matter of sign only.

Note: from this section on, the notation $\Delta\mathbf{v}$ stands for an increment in chaser absolute velocity and it does not refer to the difference $\mathbf{v}_t - \mathbf{v}_c$, but to the difference in chaser's velocity before and after an impulsive maneuver.

Maneuvers are assumed to be impulsive. Typical $\Delta\mathbf{v}$ s values for formation keeping approximately amounts to 10^{-3}m/s . This justifies the assumption, since hydrazine thrusters (which chaser will be equipped with) can perform such maneuvers time interval of less than 1s. In [41] an impulsive control scheme is presented. The main benefit to control a formation flying by means of impulsive maneuvers lies in the capability to correct desired orbital elements without undesired changes in other ones. In near-circular close orbits one of the main needs is to correct the argument of perigee and the mean anomaly, minimally impacting the remaining orbital elements. Indeed, as presented in Section 2.2.1, orbit locations where impulsive maneuvers are performed play a primary role in obtaining only the desired changes. Flight results of mission such PRISMA [?] show the reliability of impulsive control model.

2.2.1 Control strategy

Using Gauss's variational equations of motion, a firing sequence is established that allows only certain orbit element errors to be corrected during an orbit with little or no effect on the remaining orbit element differences. However, Gauss's variational equations of motion are derived for osculating orbit elements. Because specific mean orbit element differences are desired, modifications are introduced to account for the small differences between mean and osculating elements. These relationships allow for a more efficient impulsive thrusting scheme to establish the desired mean orbit element differences faster. Whereas this impulsive feedback control is demonstrated and applied to the spacecraft formation flying problem, it can also be applied to the general orbit correction problem [41].

Considering impulsive maneuvers and relative state as described in 2.24, as presented in [2], variational equations can be re-written in order to express the relationship between an instantaneous velocity increment and the consequent increment in ROE. This set is easily obtainable by considering that, before and after a maneuver, absolute position does not change and the velocity increment is the result of an average acceleration, $\bar{\mathbf{f}}$, impressed in a short time interval $t_M^+ - t_M^-$:

$$\Delta \mathbf{v}_C = \int_{t_M^-}^{t_M^+} \mathbf{f} dt \approx \bar{\mathbf{f}} (t_M^+ - t_M^-) \quad (2.49)$$

If the relative state is considered to be the state of the target with respect to the chaser, then the velocity increment seen by the target will be the opposite of the one performed by the chaser.

$$\Delta \mathbf{v}_C = -\Delta(\delta \mathbf{v}) \quad (2.50)$$

$$\delta \mathbf{r}(t_M^+) = \delta \mathbf{r}(t_M^-) \quad (2.51)$$

$$\delta \mathbf{v}(t_M^+) = \delta \mathbf{v}(t_M^-) + \Delta(\delta \mathbf{v}) \quad (2.52)$$

where $\Delta(\delta \mathbf{v})$ is the relative velocity increment seen by the target, i.e. is the increment in velocity of the target relative velocity wrt the chaser. An increment in velocity causes an increment in relative orbital elements:

$$\Delta(a\delta\alpha) = \frac{1}{n} \begin{bmatrix} 0 & 2 & 0 \\ -2 & 0 & 0 \\ \sin u_M & 2 \cos u_M & 0 \\ -\cos u_M & 2 \sin u_M & 0 \\ 0 & 0 & \cos u_M \\ 0 & 0 & \sin u_M \end{bmatrix} \Delta(\delta \mathbf{v}) \quad (2.53)$$

From Eq.2.53 it is clear how the location on the chaser's orbit affects the obtained

relative orbital elements variations. The same velocity increment is split differently depending on the value of u . It is intuitive that relative mean argument of latitude regards only relative eccentricity and inclination vectors variations. Moreover, relative mean longitude seems to be affected only by radial component of maneuvers but along-track Delta-vs actually affect $a\delta\lambda$ since a tangential thrust increases the semi-major axis and then the relative semi-major axis as well, which causes the already mentioned along-track drift.

The control scheme adopted for this study has been widely adopted and tested, especially in TANDEM-X mission ([42] and mainly in [25]), and it consists in relative orbital elements corrections only by mean of T and N Delta-vs. By assuming such delta-vs distribution [26], maneuver locations for in-plane and out-of-plane control are

$$\tan u_{M(T)} = \frac{\Delta(\delta e_y)}{\Delta(\delta e_x)} \quad (2.54)$$

$$\tan u_{M(N)} = \frac{\Delta(\delta i_y)}{\Delta(\delta i_x)} \quad (2.55)$$

For what concerns cross-track direction, one maneuver is enough to reset the relative inclination vector. For in-plane delta-v component, a distribution of the total delta-v in two maneuvers is preferred. Indeed, especially in formation keeping, relative semi-major axis needs to be as closest as possible to zero. An efficient method to divide the $\Delta(\delta v_T)$ is presented in [2] where relative semi-major axis variation is used in order to force the along-track drift and then it is reset to zero. Eq.2.56 shows the delta-v distribution and Figure 2.11 illustrates an example of desired trend for relative semi-major axis δa , relative mean argument of latitude δu and relative argument of perigee φ .

$$\Delta(\delta v_T)_1 = \frac{n}{4}(\Delta(a\delta a) + \Delta(a\delta e)) \quad (2.56)$$

$$\Delta(\delta v_T)_2 = \frac{n}{4}(\Delta(a\delta a) - \Delta(a\delta e)) \quad (2.57)$$

$$u_{M1} = \arctan \frac{\Delta(\delta e_y)}{\Delta(\delta e_x)} \quad (2.58)$$

$$u_{M2} = u_{M1} + \pi \quad (2.59)$$

The strategy adopted considers a control period, usually a multiple of the chaser's orbital period, in order to perform periodic checks and maneuvers. The control Period T is computed so that the drift of ROEs can be bounded in a desired region, as shown in Figure 2.11 and Figure 2.12.

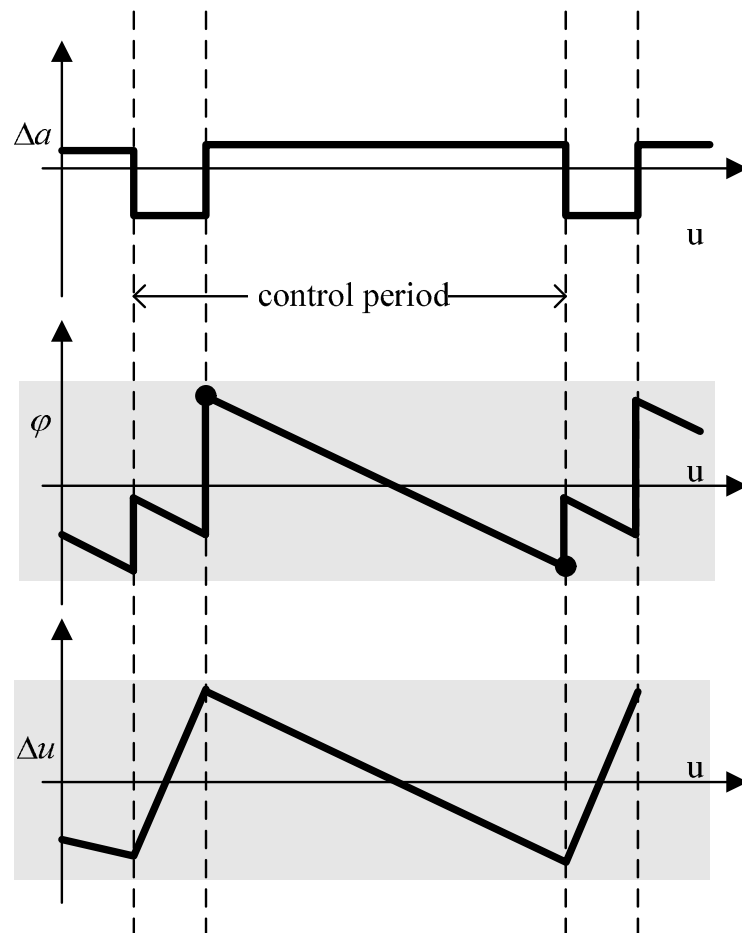


Figure 2.11: Drift within a control period

Relative semi-major axis is kept as much as possible in the proximity of zero. Grey stripes in relative perigee and relative argument of latitude indicate the region in which drifts are allowed. The drift reaches the boundaries at the end of each control cycle

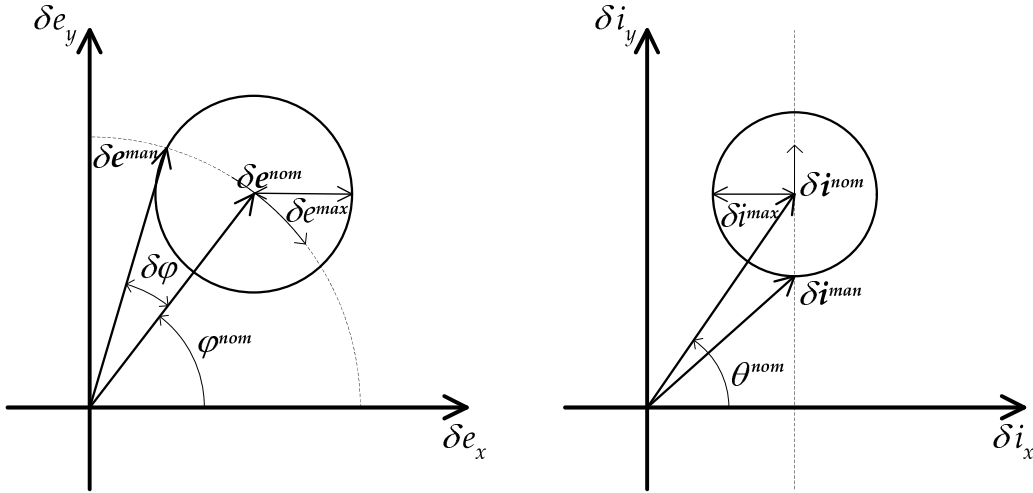


Figure 2.12: Tolerance windows for relative eccentricity and relative inclination

Relative eccentricity and relative inclination vectors drift in time as shown in Figure 2.9. The control tolerance is then computed on these drift rates. Superscripts in Figure 2.12 indicate the desired nominal value ("nom" on which the control window is centered), the upper limit of the control tolerance (the maneuver is needed when a maximum value, "max", is reached) and the value to restore after the execution of the maneuver ("man"), in order to start another control cycle.

2.2.2 Passive safety

Navigation at close-range involves risk of collision. Whichever the nominal formation, a passive safe configuration should be considered. Successfully tested in TanDEM-X mission [43], a safe approach is to set ROEs to get an helix-shape trajectory. As explained in [2], minimum cross-track distance is proportional to the scalar product of relative eccentricity and relative inclination vectors.

$$\delta r_{RN} = \sqrt{\delta r_R^2 + \delta r_N^2} \quad (2.60)$$

$$\delta r_{RN} \propto \delta \mathbf{e} \cdot \delta \mathbf{i} \quad (2.61)$$

Then, by maximizing the magnitude of the scalar product, the minimum distance on cross-track plane is maximise as well. A safe bound configuration can consider a ROE set as:

$$a\delta\alpha = [0 \ 0 \ 0 \ a\delta e_{y,nom} \ 0 \ a\delta i_{y,nom}]^T$$

2.3 Estimation

The guidance and control laws require the accurate knowledge of the relative orbit elements of the formation, that is indeed where the focus of this study lies. The controller needs to receive as input relative orbital elements computed with mean orbital elements in order to properly perform formation maintenance. Measurements by on-board sensors are taken into account in the simplified dynamical model within the observer, in order to estimate the relative state. Line of sight and range information can be linked to relative position by trigonometric relationships in chaser's RTN frame. Of course, camera and radar will have their own frame on-board the satellite and will not coincide with the RTN one. It is relevant for this study to understand how to handle relative navigation while it is not considered the issue - of primary relevance too - of relative attitude. For this reason, since no focus on relative attitude is pursued and any local frame can be led back to the local RTN frame, only the latter is considered.

Since knowing current formation relative state is essential to control maneuvers, the usage of an on-board real time dynamical filter is mandatory. Thanks to the dynamical model, the filter can rely on the simplicity and rapidity of execution for the computation. A dynamical filtering of the relative orbit elements is done using a discrete EKF. Kalman filter is indeed an optimal observer [44].

A linear observer cannot be used: Eq.2.40 provides a linear transition law but measurements cannot be related to the relative state with a linear relationship, as described in Section 2.3.2. Orbital elements are affected by time variations on different scales. Perturbations determine secular variations but orbital elements experience short and long period variations too. In order to maintain a desired formation, the GNC system needs to control the mean orbital elements. In this sense, the model implements osculating to mean and mean to osculating conversions, according to Brouwer theory [45] and its further developments. Performing ROEs state transition is not affected by the osculating to mean elements conversion, since the transition matrix operates with mean orbital elements. The measurement model is instead affected by these conversions: measurements detect current relative position, which are related to target's and chaser's absolute position vectors and so to osculating orbital elements. For this reason, osculating to mean and viceversa conversions within the filter are needed.

2.3.1 EKF formulation

Kalman filter estimates the state of a system by means of a recursive prediction-correction loop. First it predicts the next state by means of a dynamical model (e.g. the transition law for ROEs), propagating the current state guess, then it corrects the prediction with measurement values coming from sensors. Constitutive equations

of discrete time EKF are gathered in Eq.2.62

$$\hat{x}_k^- = f(\hat{x}_{k-1}, u_k, 0) \quad (2.62)$$

$$P_k^- = A_k P_{k-1} A_k^T + W_k Q_{k-1} W_k^T \quad (2.63)$$

$$(2.64)$$

$$K_k = P_k^- H^T (H_k P_k^- H_k^T + V_k R_k V_k^T)^{-1} \quad (2.65)$$

$$\hat{x}^k = \hat{x}_k^- + K_k (z_k - h(\hat{x}_k^-, 0)) \quad (2.66)$$

$$P_k = (I - K_k H_k) P_k^- (I - K_k H_k)^T + K_k R_k K_k^T \quad (2.67)$$

where the covariance P_k has been computed in a more stable form [46] (Joseph stabilized form [47]). Figure 2.13 shows the recursive sequence followed by the filter.

Functions f and h are the transition and the measurement functions respectively. The reason why an additional null input for both is considered is the presence of noise, such as these are included in functions: $f(x, u, w)$ and $h(x, \nu)$. Transition is affected by process noise, i.e. uncertainties introduced by the mathematical model of a real phenomenon. Measurement model is affected by measurement errors since sensors are not perfect. Both process and measurement noise are considered to be zero-mean, white and uncorrelated, i.e. the probability distribution p is assumed to be normal, such that

$$p(w) = N(0, Q)$$

$$p(\nu) = N(0, R)$$

where Q and R are process and measurement covariances respectively. The assumption of normal distributed noises makes impossible for the filter to consider systematic errors and biases, unless these are considered within the state to be estimated.

Since the EKF is a linearisation of the non-linear state equations around the expected value, first order time partial derivatives of functions f and h need to be

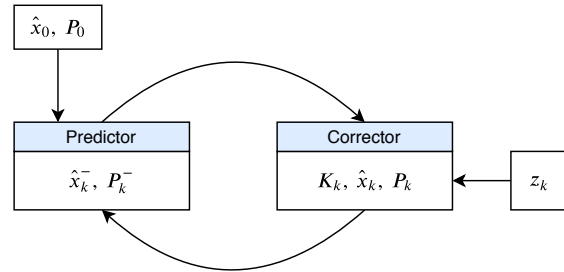


Figure 2.13: Predictor-corrector EKF loop

The predictor must be initialized (initial conditions x_0, P_0). The measurement corrector takes as input measurements z_k at time t_k .

taken with respect to the state and the noise.

$$A = \frac{\partial f}{\partial x} \quad W = \frac{\partial f}{\partial w} \quad H = \frac{\partial h}{\partial x} \quad V = \frac{\partial h}{\partial v} \quad (2.68)$$

Note: it follows that the state x coincides with the ROEs dimensional set (Eq.2.30) and A coincides with Φ (Eq.2.40).

2.3.2 Measurement model

Measurements z are provided by line-of-sight and range sensors. For the first, enough knowledge is available thanks to the heritage of AON, but for the latter, less is known about behaviour in such scenarios. This implies a more accentuate attention on different possible values to adopt for measurement noise. Line-of-sight noise can be assumed to be less than 1° .

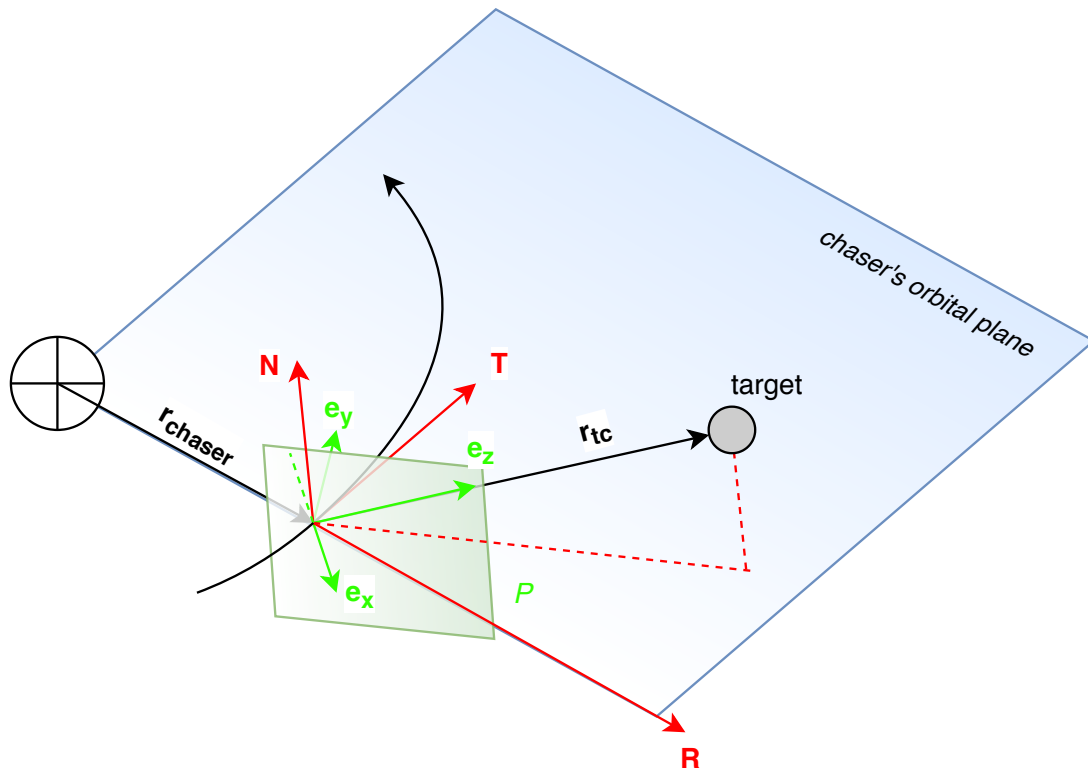


Figure 2.14: RTN frame and relative position

The union of LOS and range measurements provides the complete measured 3D relative position. Figure 2.14 recalls the position of the target with respect to chaser in RTN frame and depicts the relative right-hand frame centered on the chaser. Unit vector e_z is the line-of-sight and it can be projected in RTN components in order to be related to relative state and ROEs.

Relative position vector can be written in RTN components in terms of measured values, which coincide with spherical coordinates. Measurement model h and relative position in spherical coordinates can be written as

$$\mathbf{h} = \begin{bmatrix} \rho \\ \alpha \\ \delta \end{bmatrix}, \quad \delta \mathbf{r} = \mathbf{g}(\mathbf{h}) = \rho \begin{bmatrix} \sin \delta \\ \cos \delta \cos \alpha \\ \cos \delta \sin \alpha \end{bmatrix} \quad (2.69)$$

Measurement model partial derivatives, i.e. of h with respect to the state x , can be written by means of the chain rule as

$$\mathbf{H} = \frac{\partial \mathbf{h}}{\partial(\delta \mathbf{r})} \frac{\partial(\delta \mathbf{r})}{\partial \mathbf{x}} \quad (2.70)$$

where $\frac{\partial(\delta \mathbf{r})}{\partial \mathbf{x}}$ coincides with the transition matrix Φ , restricted to the first three rows. The other partial derivative can be analytically computed ($\delta \mathbf{r} = [\delta r_R \ \delta r_T \ \delta r_N]^T$ has been replaced with $y = [y_R \ y_T \ y_N]^T$, to make the notation easier to read) as

$$\frac{\partial \mathbf{h}}{\partial \mathbf{y}} = \begin{bmatrix} \frac{\partial \rho}{\partial y_R} & \frac{\partial \rho}{\partial y_T} & \frac{\partial \rho}{\partial y_N} \\ \frac{\partial \alpha}{\partial y_R} & \frac{\partial \alpha}{\partial y_T} & \frac{\partial \alpha}{\partial y_N} \\ \frac{\partial \delta}{\partial y_R} & \frac{\partial \delta}{\partial y_T} & \frac{\partial \delta}{\partial y_N} \end{bmatrix} \quad (2.71)$$

$$\frac{\partial \mathbf{h}}{\partial \mathbf{y}} = \begin{bmatrix} \frac{y_R}{d} & \frac{y_T}{d} & \frac{y_N}{d} \\ 0 & \frac{-y_N}{y_T^2 + y_N^2} & \frac{y_T}{y_T^2 + y_N^2} \\ \frac{\sqrt{y_T^2 + y_N^2}}{d^2} & -\frac{y_R y_T}{d^2} \frac{1}{\sqrt{y_T^2 + y_N^2}} & -\frac{y_R y_N}{d^2} \frac{1}{\sqrt{y_T^2 + y_N^2}} \end{bmatrix} \quad (2.72)$$

where $d^2 = y_R^2 + y_T^2 + y_N^2$.

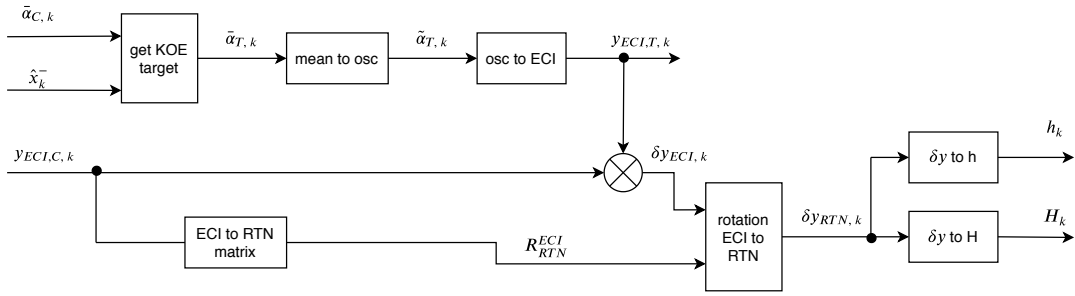


Figure 2.15: Block scheme of the filter's measurement model

Please refer to Appendix B for the complete scheme of the filter. Here only the measurement model is deepened here. After the a priori estimate of the system state, i.e. the prediction, measurement model receives in input the known absolute state, $y_{ECI,c}$, and mean orbital elements, $\bar{\alpha}_c$, of the chaser (both known thanks to GPS) and the a priori prediction, \hat{x}^- . Through relative orbital elements, it is possible to compute mean orbital elements of the target. To get the absolute state in ECI frame it is necessary to operate mean-to-osculating conversion. Once the absolute state is obtained, relative state in ECI frame can be computed. then, by rotating to RTN, measurement model $h(x_k^-)$ and measurement derivatives H_k are computed. In Figure 2.15 the architecture of the measurement model within the filter is depicted.

Chapter 3

Simulation environment

3.1 simulation baseline

The simulation is setup in Matlab Simulink environment, with the auxilium of external libraries. Orbit propagation for a non-Keplerian motion is considered and transformation from osculating to mean orbital elements (and viceversa) is needed. For these reasons, the model implements libraries by Montenbruck-Gill [3] and functions taken from open source NASA GSFC General Mission Analysis Tool (GMAT).

The model architecture is a feedback-loop controller. The controller receives the nominal set of the formation and it is fed with the estimation of the current relative state of the target with respect to the chaser, then impulsive manoeuvres are performed. Orbit propagation follows and both chaser's and target's absolute state are computed. The relative state is observed through measurements generation, the relative state is estimated by an observer and sent to the controller again.

Orbit propagation takes into account perturbations, as higher order terms of the gravitational fields, atmospheric drag and solar radiation pressure, as well as eclipse periods. The propagation gives a numerically integrated result, representing the reference of the model. This reference reflects what is “actually” happening in orbit. From this reference, measurements are modelled and used to estimate the relative state. The controller computes the discrepancy between the estimated relative state and the nominal set with a constant control period. In each control window, manoeuvres are computed in order to fill this gap, considering also the drift that the formation will see before the computed manoeuvre is executed, as discussed in Chapter 2.

Manoeuvres are affected by execution errors of 1mm/s-10mm/s circa and are simply modelled as velocity increments, since it is reasonable to assume that time interval needed to fire the thrusters is less then the simulation step – about 10 seconds. It is important to note that attitude correction is not taken into account, and the manoeuvres required concern only the GNC aspect. Measurements are

modelled based on the dynamical reference output. Therefore, line-of-sight measurements are noisy angles of target orientation with respect to the chaser frame and range measurements are noisy values of the relative distance. In particular, line-of-sight measurements are modelled thanks to an images generating server. Target's position in images is computed by taking the average of the illuminated pixels. Then, rotating from sensor's frame to RTN chaser's frame, the line-of-sight angles are computed. Such modelled measurement experiences a more refined noise, since measurements are not generated by simply adding gaussian and biased noise to the dynamical reference. Moreover, chaser's absolute position and velocity is assumed to be known since it can rely on GPS signals. This is also modelled starting from the dynamical reference. The estimation is performed by mean of a dynamical filter. Since the problem is nonlinear, the Extended Kalman Filter (EKF) is implemented. The filter predicts the relative state with the first order simplified model of the relative motion, described in Chapter 2. The prediction is then updated with measurements. This is possible by expressing the relationship between the measurements – i.e. relative orientation and distance - and the relative state, through a measurement model. In this feature relies the contribution of this study. In figure 3.1 the simulation environment is conceptually sketched.

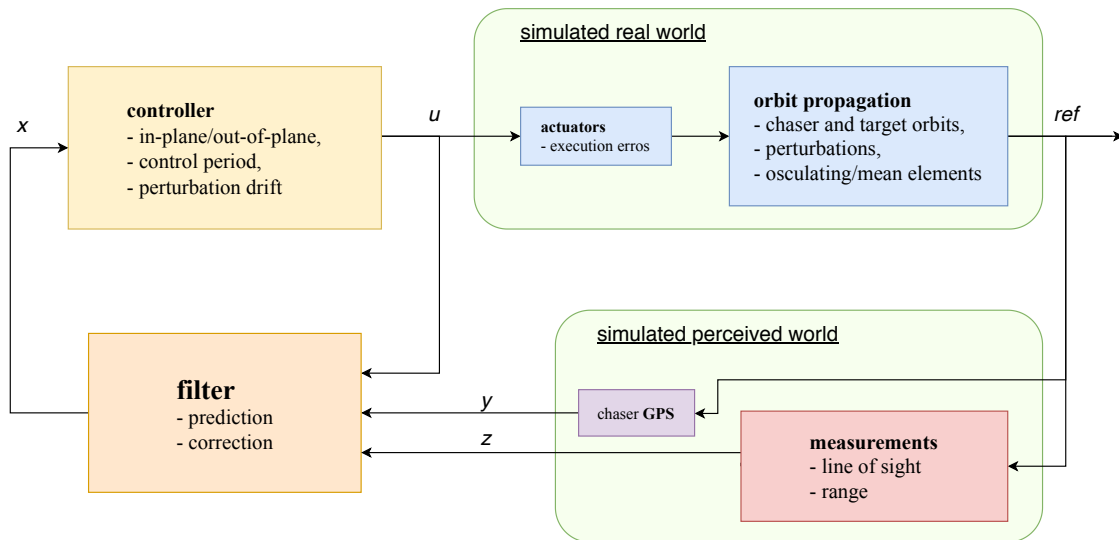


Figure 3.1: High level simulation environment layout

3.2 Images generation

LOS measurements are simulated by means of images generation.

Note: The chaser is assumed to be always oriented toward the target, i.e. the camera c_z axis always coincides with the unit vector from the chaser center of mass to the target center of mass.

An S-Function is implemented within the LOS measurement generator block and is connected to a image generation server, designed by Jean-Sébastien Ardaens (DLR). The function f_{img} outputs the measured line-of-sight unit vector pointing the target, having received in input:

- chaser's absolute state vector in ECI frame,
- chaser's attitude quaternion in ECI frame,
- target's absolute state vector in ECI frame,
- target's attitude quaternion in ECI frame,
- simulation time.

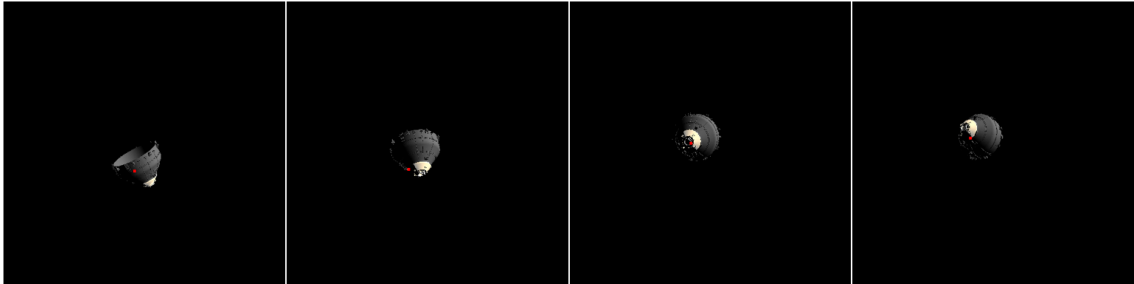


Figure 3.2: Examples of generated images and computed centroids

$$\mathbf{u}_{ECI} = \mathbf{f}_{img}(\mathbf{y}_{ECI,chaser}, \mathbf{q}_{ECI,chaser}, \mathbf{y}_{ECI,target}, \mathbf{q}_{ECI,target}, t)$$

The position of the target in the image is computed by averaging illuminated pixels to find the centroid of the target. It does not coincide with the target's center of mass. Here lies the measurement noise. Since the target is moving and tumbling with respect to the chaser, it reflects light in different ways, making challenging the identification of the center of mass. The closer is the target, the bigger it appears to the chaser and the greater the misalignment of the measured LOS direction may appear. At far range indeed, reflections does not imply a noisy measure since the target is approximately a point. The maximum angular error that can be committed is related to the distance and the size of the object. Figure 3.3 shows the maximum angular error at a given distance. Note that $\tan \varepsilon = \frac{D/2}{r}$. This topic is well described

in [27]. As described in Section 1.4, AON has been widely deepened through studies and in-orbit demonstrations. The image server inserted in the simulation relies on such knowledge. Figure 3.2 shows a sequence of images generated by the server during a simulation.

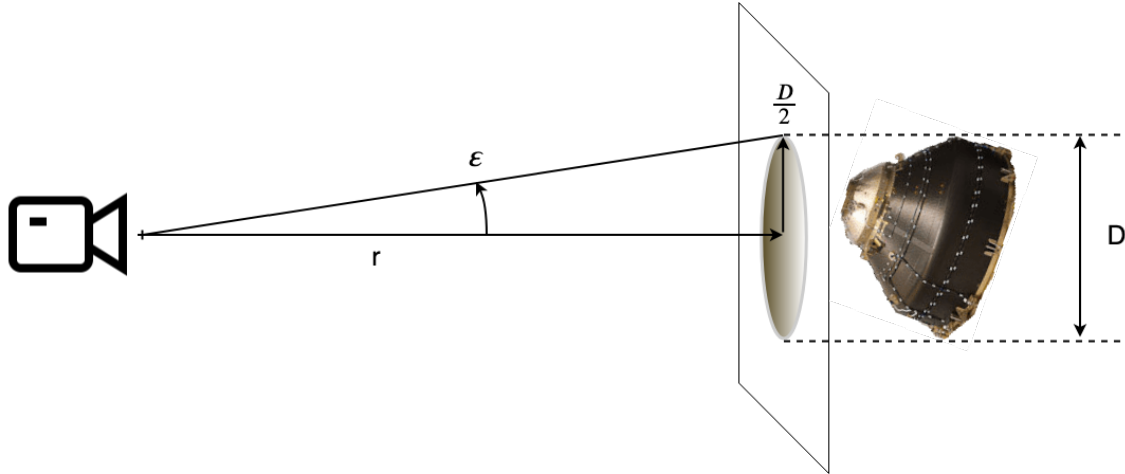


Figure 3.3: Misaligned centroid: maximum angular error seen by the on-board camera

3.3 Range measurements

Range measurement are generated from the dynamical reference too. However, no server is available in order to generate a more realistic set of measurements, then these ones are modelled as noisy values.

LOS camera gives as output the value of two angle, and is assumed that every error in local bearing and elevation is due to line-of-sight and not to range measurement. Instead, range can vary along the radial direction. Therefore, a noisy radar measurement may result in a different range value, but still lying on the same direction. in Table 3.1 typical values adopted during simulations are pointed out. It is crucial to know that values greater than 0.5 m may probably compromise are not recommended if accuracy at the meter level is to be achieved.

measurement parameter	perfect				noisy			
$\sigma_r[m]$	0	0.2	0.8	1				
$b_r[m]$	0	0	0.5	0.5				

Table 3.1: Standard deviation and bias for range measurement

3.4 Maneuver execution errors

Within the simulation, maneuver execution errors can be considered as a maximum error on the delta-v magnitude of 3% and a misalignment of about 1° . Such errors reflect the real situation of an hydrazine thruster with maneuvers executed periodically - i.e. about 1 maneuver each 1 to 3 days. The scenarios can be considered similar to that described in the TAFF system in [42]

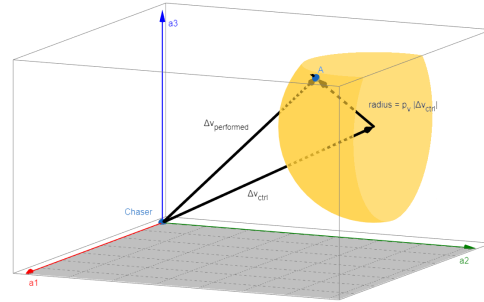


Figure 3.4: Maneuver execution error: $\Delta \mathbf{v}$ uncertainty sphere

Chapter 4

Simulation results

In this Chapter, results of one among the analyzed scenarios are reported, where the chaser aims to reach a nominal close formation flying. First, the initial transient is discussed and the effect of convergence. Then, three time intervals are considered:

- formation reconfiguration, from mid-range to close-range,
- the onset of a filter divergence and convergence recovering,
- close-range formation keeping.

4.1 Convergence

An initial ROEs set of $\mathbf{x}_0 = [-5, 10, 10, 12, -8, 20]^T$ is considered, with an initial filter error guess of $\Delta\mathbf{x} = [3, -20, 8, 10, 10, 15]^T$. In Figure 4.1 the initial convergence can be appreciated.

It is reasonable to allocate a period for the convergence of the filter before starting the control sequence.

4.2 formation reconfiguration and keeping

In Figure 4.2 three moments can be observed. After the initial filter convergence, the controller tries to reconfigure the formation to set the nominal values. Nominal formation has been defined as $\mathbf{x}_{nom} = [0, 30, 5, -20, 5, -20]^T$.

Figures 4.4 and ?? show the estimation error and the residuals respectively.

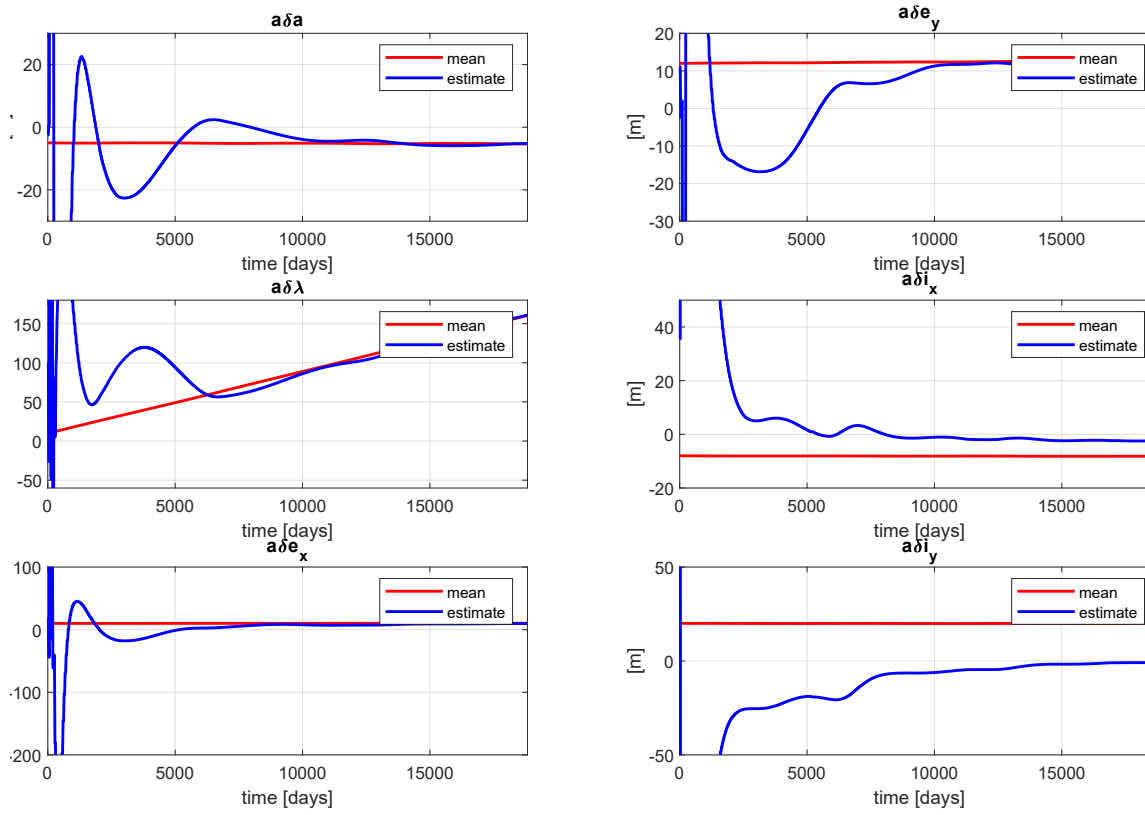


Figure 4.1: Convergence during the initial period (18000 s, about 5 hours)

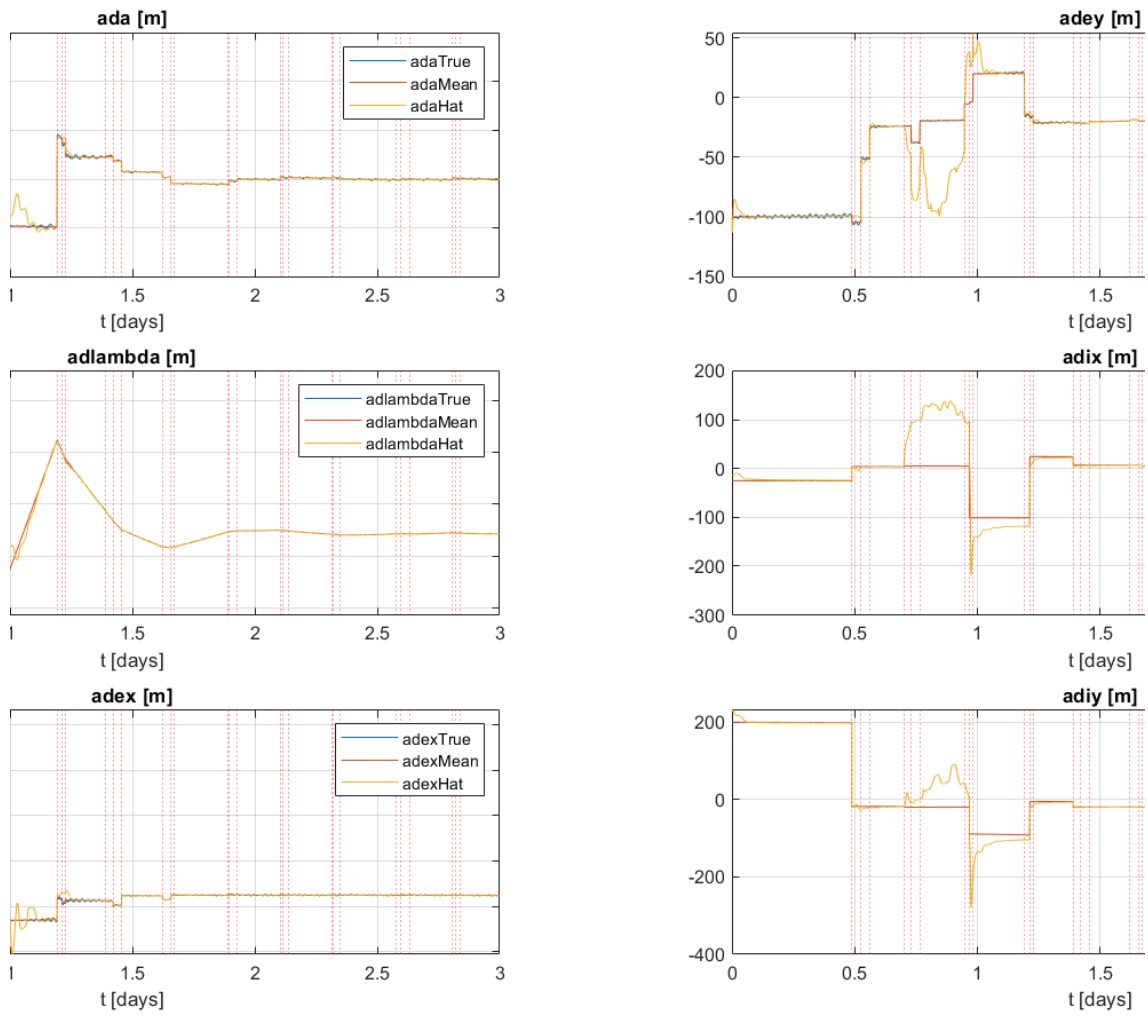


Figure 4.2: scenario 01, ROE evolution

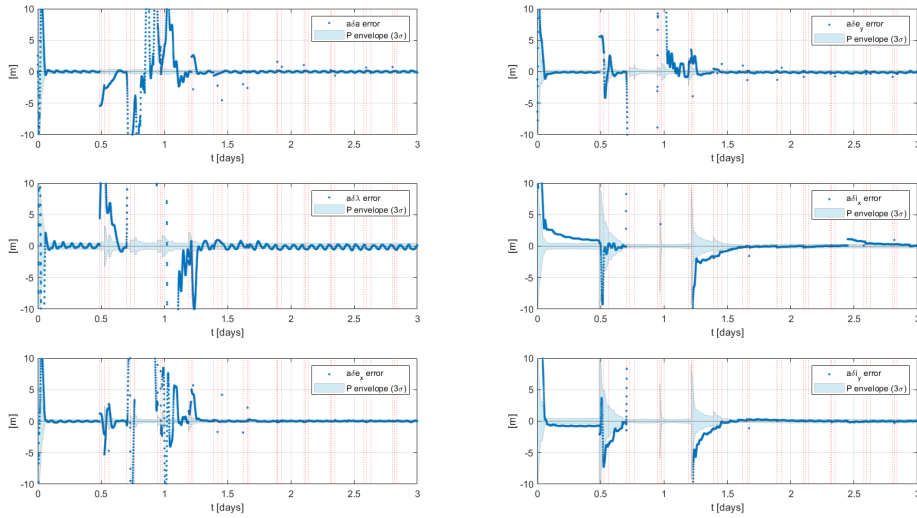


Figure 4.3: scenario 01, error

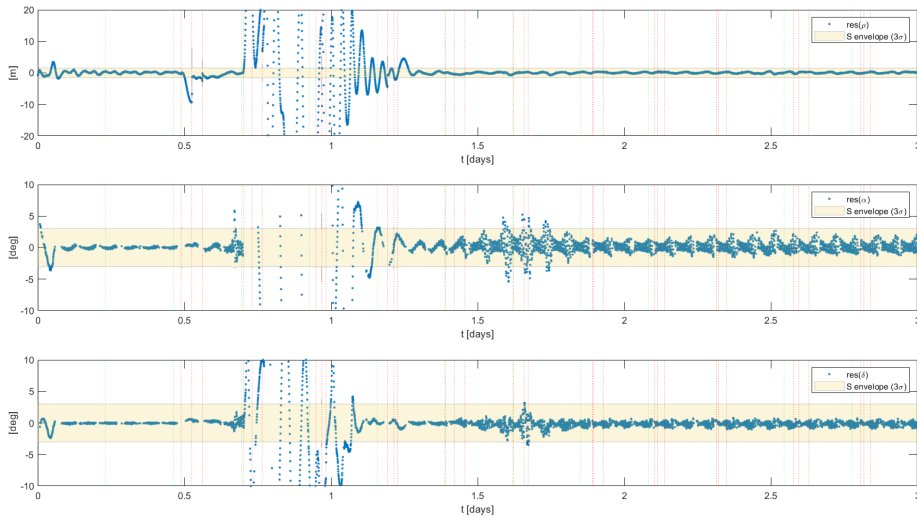


Figure 4.4: scenario 01, residuals

After about 17 hours, i.e. 0.7 days, instability occurs. This occurs first in relative inclination components and then, since state transition matrix relates relative inclination x-component to the evolution of the other ROE, all the other elements start to diverge. This is most probably due to the weak capability of relative inclination x-component's covariance to update in time. Indeed, this part of the covariance converges slower than the other contributes. This leads the relative inclination to be susceptible of fast changes.

After that, convergence is recovered in a wider time interval. In Figures 4.4 and ?? the periodic control sequences can be appreciated. Indeed, the fact that residual remain inside 3σ covariance envelope, means that the filter is able to predict and correct properly the system state and the close formation can be ensured with an estimation error at meters level.

4.3 Out-of-plane: no fast convergence

both in formation keeping and formation reconfiguration, it may occur that estimation of ROE element $a\delta i_x$ presents instabilities that force the estimate to move away from the already reached convergence. Sometimes after another transient, the estimate goes back and all the filter converge. But it could be even that such instabilities lead the filter to diverge.

One reason why $a\delta i_x$ is susceptible of such phenomena lies on its transition matrix. Indeed, such behaviour can be recognized even in predictor-only mode of the filter, i.e. without updating the estimate with the measurements. Figure 4.5 shows the convergence of P covariance envelopes. The wider the envelope, the greater the allowed ROE error. And the slower the envelope to converge, the longer wide errors will persist, making challenging to properly control the formation.

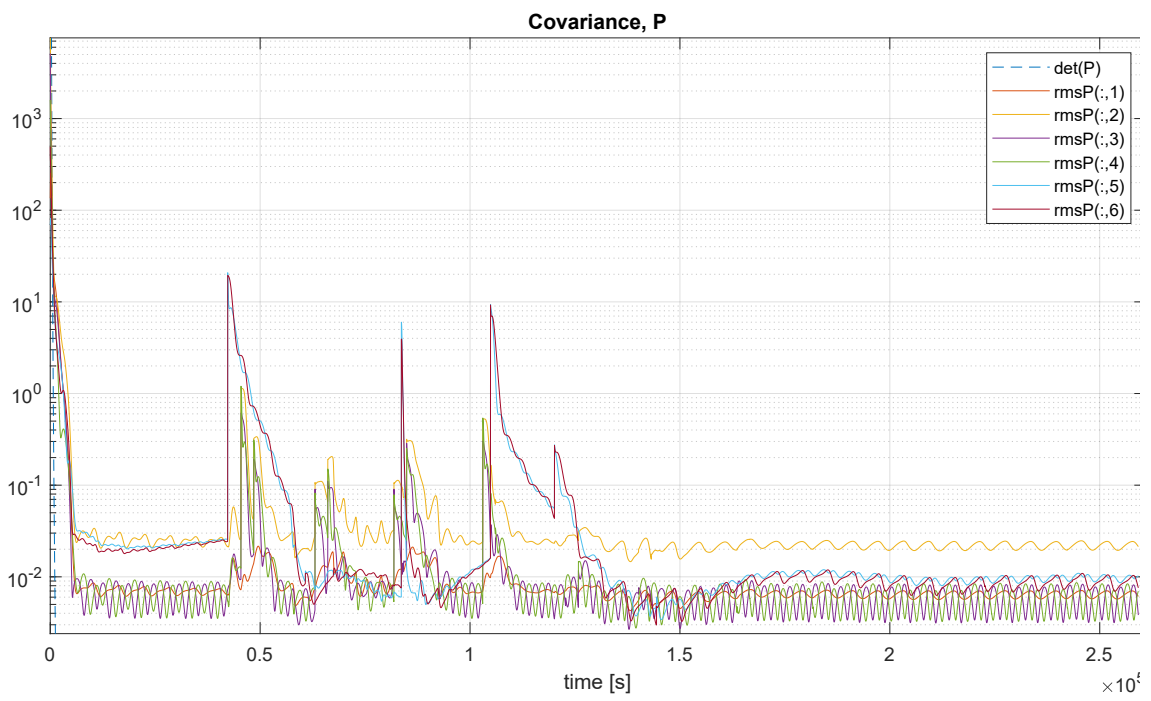


Figure 4.5: Covariance envelop amplitude for each ROE

4.4 Covariance, P

All the errors due to simulation (delays, manoeuvre shifts, transformation inaccuracies such as OscMean...), that cannot be analytically explained (or for which it would take too long to have the analytic expressions of all errors) could be considered from the filter covariances. By assuming to have constant process and measurement covariances Q,R, the estimation covariance P can consider the error on the filterInputs. Time update of $P_k = AP_k^- A^T + Q + P_{\Delta v} + P_{uM}$ then increases the covariance envelope in in correspondence of a maneuver. Are taken into account:

- maneuver execution errors: Delta-v executed is not equal to the Delta-v required,
- maneuver execution location: due to simulation time, a maneuver may be performed a little advance or late than the requested location.

4.5 Recommendations

Some recommendation may be suitable.

- close formation keeping is possible, but still measurement noise must be constrained as $\sigma_b < 1m$ and $b_r < 0.3m$ approximately.
- close formation keeping is possible but it is crucial to choose of an initial state. This aspect should be more investigated.

4.6 Further development

There are mainly two topics that can be developed more in future: the dynamical model and the modelling of radar measurement.

For the first, many studied have been done in recent years to overcome limitations imposed by the CW solutions, i.e. almost circular orbit. Discussion can be found in works as [48] [49]. improvements can be ensure by adopting more precise methods, such as elliptical orbit.

The other suggestion regards the range measurement model. to get more realistic results, the range measurement could be modelled with possible noise in every direction and not only on range true-line.

Appendix A

Control algorithm

In Figure A.1 control logic flowchart is shown. The control procedure is performed periodically, with a period equal to T . Indeed, control windows start at each simulation time value t_k that is an integer multiple of the control period. Then, the state error is computed. The controller works directly on ROEs and receive as input the current deviation from the nominal set. Orbit propagation is considered in order to center the elements' drift around the nominal values: recovering the error computed at t_k is not enough to properly restore the formation. Since the state varies with time within the control window, The first order model provides a linear drift law for ROEs and this can be used in order to center state elements on the nominal value approximately in the middle of the control window, i.e. after $T/2$. Flowchart in Figure A.1 shows the adopted control logic:

- the controller receives the state estimation $\hat{\mathbf{x}}$,
- state error, $\hat{\mathbf{x}} - \mathbf{x}_{nom}$, is computed,
- state variations, $\Delta\mathbf{x}$, are computed, in order to let the state drift and reach the nominal set in the neighborhood of an half control window,
- $\Delta\mathbf{v}$ components (Δv_{T1} , Δv_{T2} and Δv_N) components and the respective maneuver locations, u_M , are computed. In-plane and out-of-plane maneuvers are independent of each other,
- the controller waits until the next maneuver location is reached, then output the $\Delta\mathbf{v}$ request to be sent to the propulsion group.

Note: Control windows need to be longer than the orbit period: indeed computed maneuver locations may require an entire orbit to be reached. A fair trade-off could be $\frac{T}{T_{orbit}} \in (3, 5)$, where T_{orbit} is the chaser's orbit period.

ROEs are then allowed to vary within tolerances. Such allowed variations depend on the system desired accuracy. The smaller the expected deviations, the more frequent maneuvers should be in order to reduce time intervals for the ROEs to drift away. Figures A.2 and A.3 show variations around nominal values for a station keeping with nominal set: $a\delta\alpha = [0, 80, 5, -20, 5, -20]^T$.

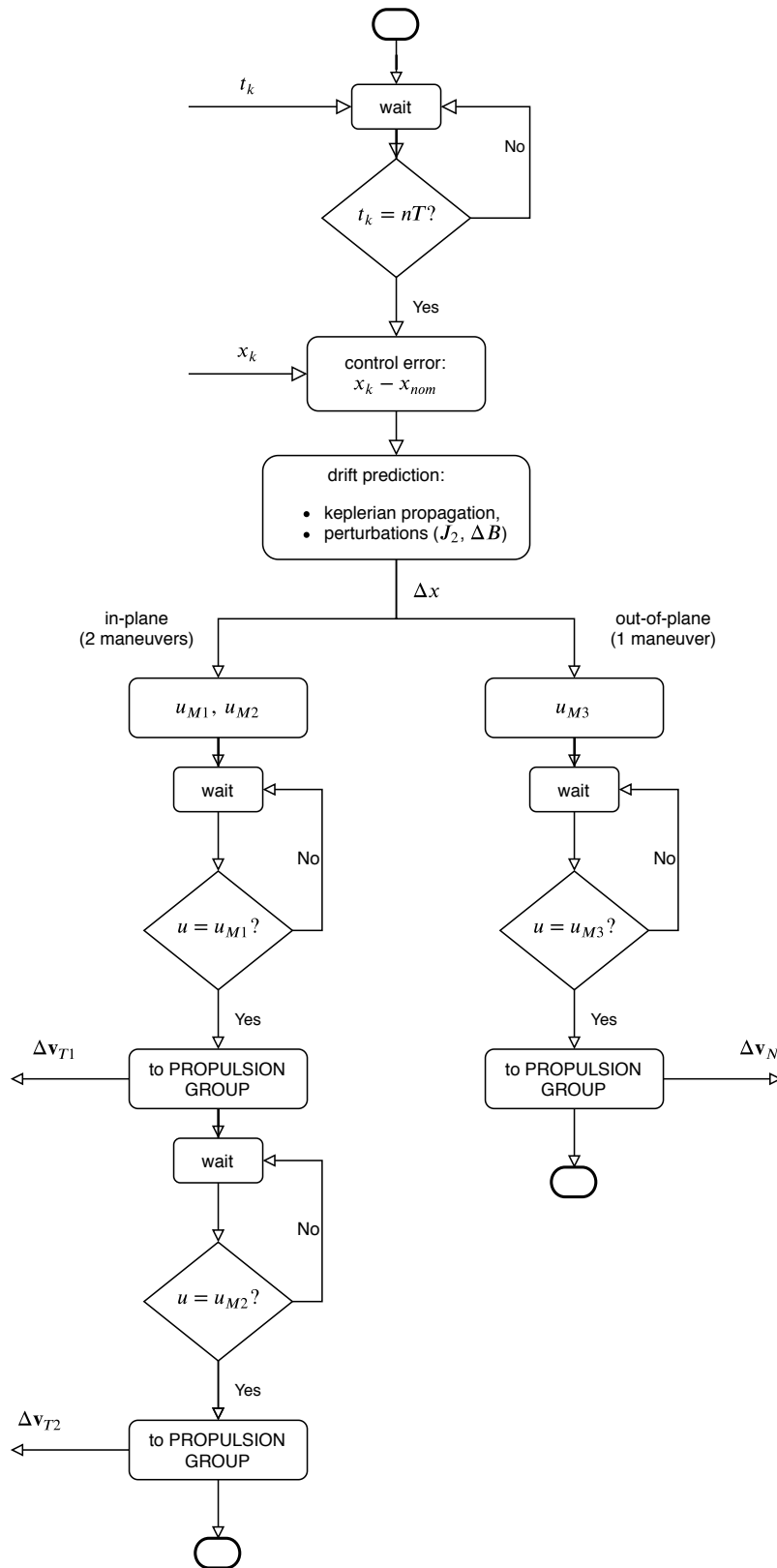


Figure A.1: Control algorithm flowchart

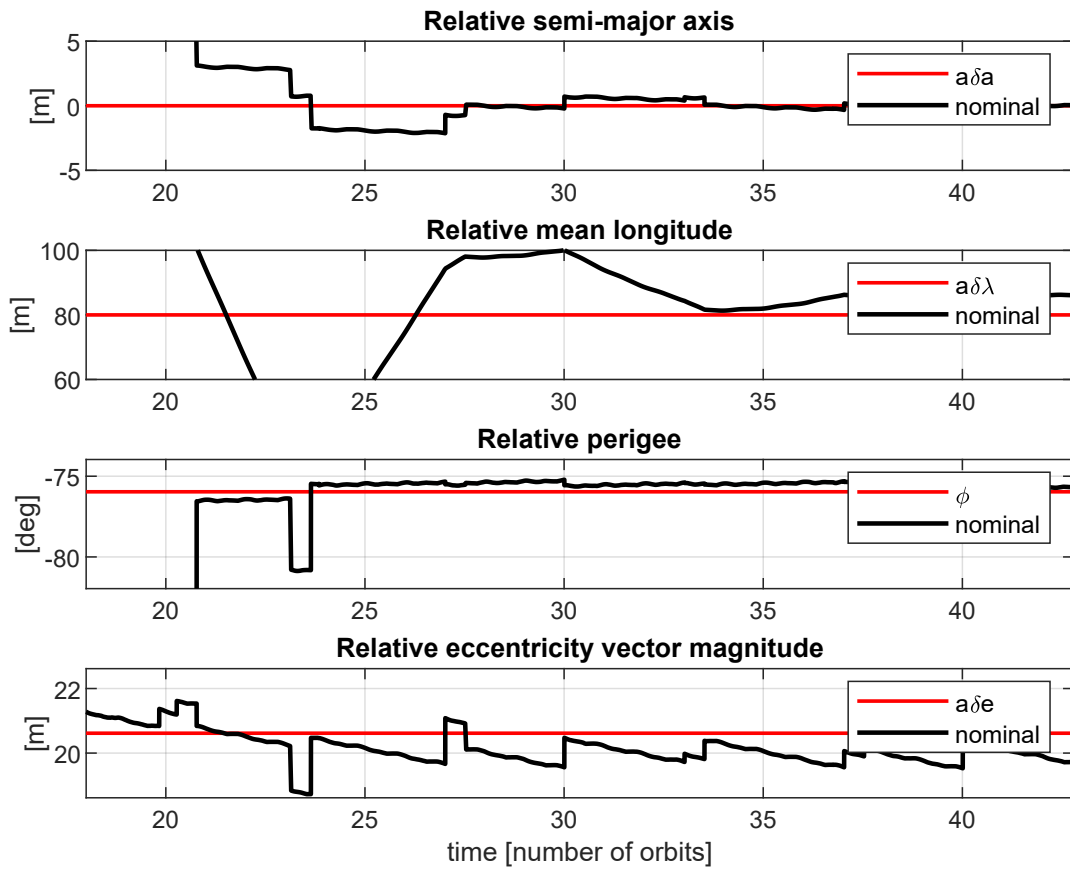


Figure A.2: In-plane control

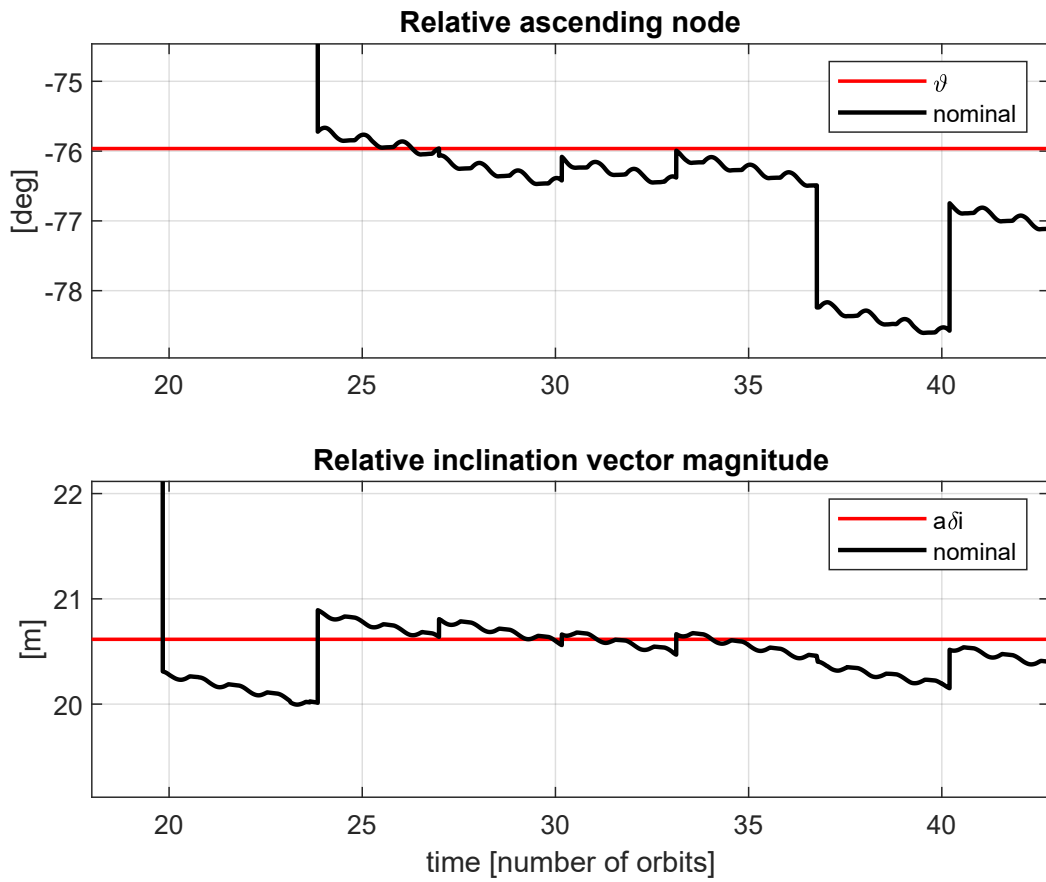


Figure A.3: Out-of-plane control

Appendix B

EKF algorithm

A block scheme showing the logic within the Extended Kalman Filter (EKF) is depicted in Figure B.1. As presented in Section 2.62, the filter estimates the state of the system, i.e. the relative motion, by two means. First, it predicts the evolution of the state in time, relying on the first order dynamical model, and then updates the prediction with measurements provided by LOS camera and the radar. The loop is so-called "predictor-corrector". The filter must be initialized with an initial guess for the state and the covariance.

Note: the initial covariance, P_0 , must be large enough to include the initial error that the filter is assuming, but not too large to cause excessive oscillations. Indeed, covariance is defined as the expected value of the state error the filter is estimating, such as

$$P_k = E[e_k e_k^T]$$

where $e_k = \hat{x}_k - x_k$, \hat{x}_k is the state estimate and x_k is the actual value of the state, which cannot be known. Then, it follows that the initial actual error $\Delta x_0 = e_0$ must be

$$\Delta x_0 < \sqrt{\text{diag}(P_0)}$$

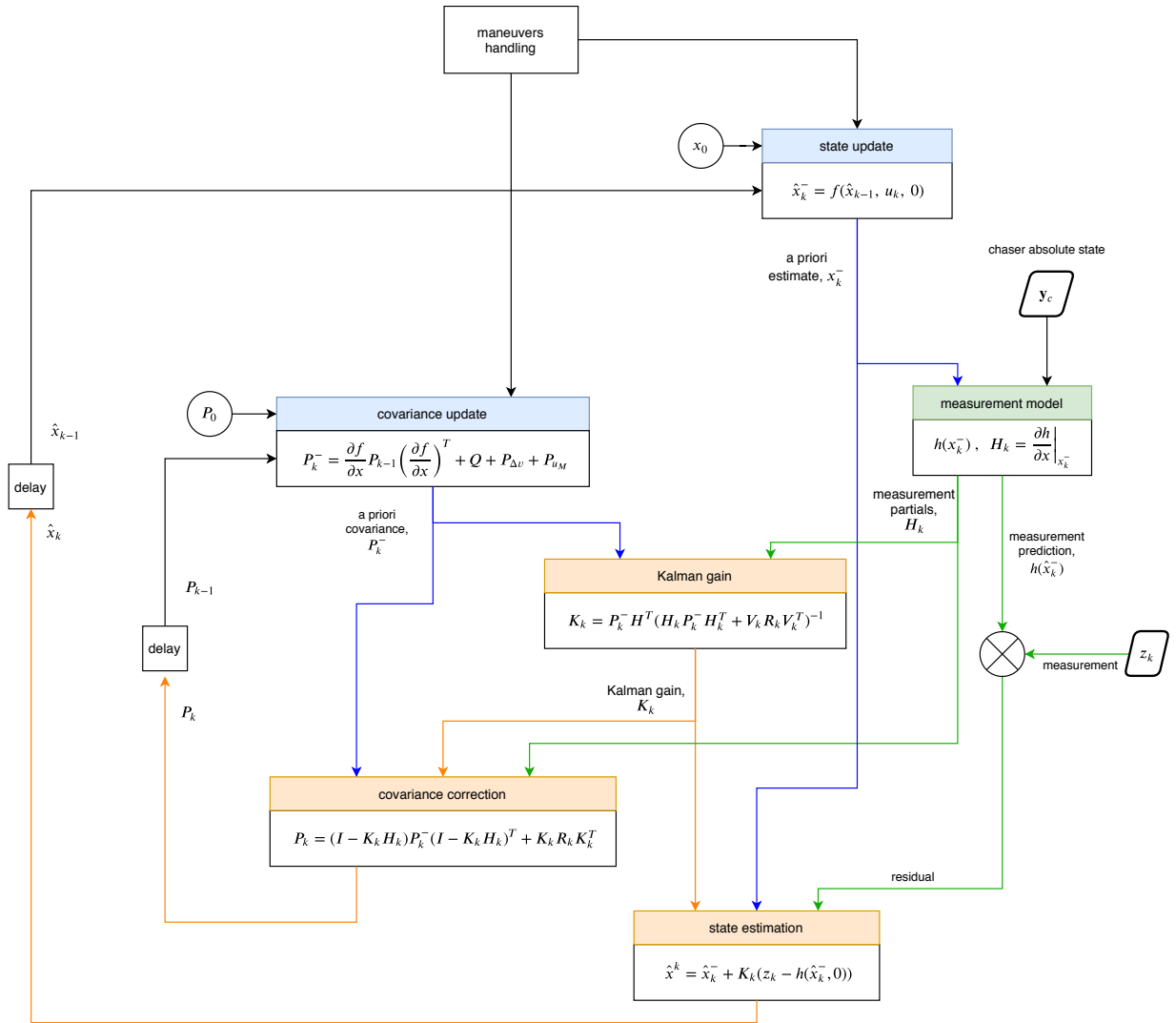


Figure B.1: Extended Kalman Filter data flow.

Appendix C

Close formation keeping

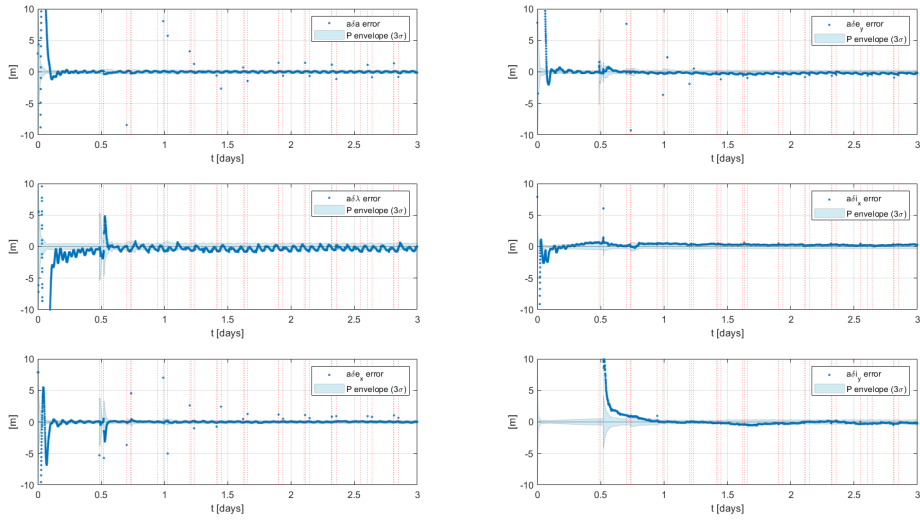


Figure C.1: scenario 02, error

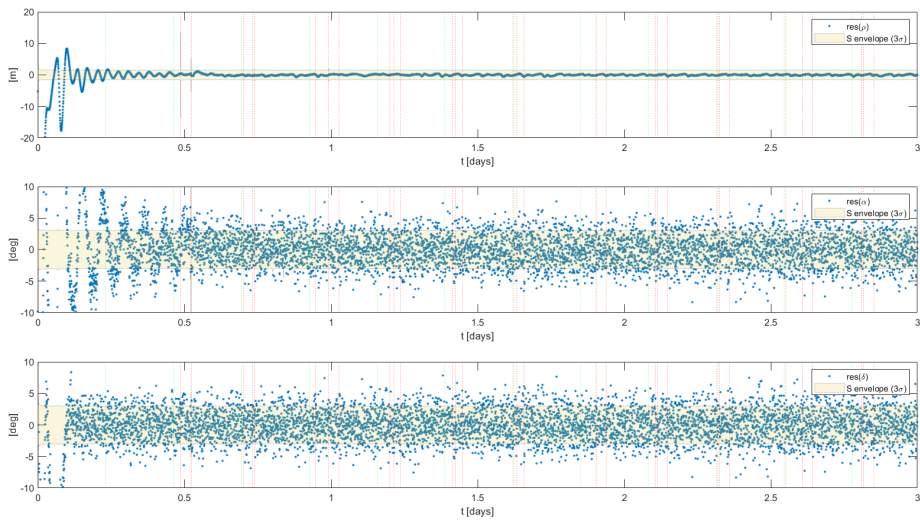


Figure C.2: scenario 02, residuals

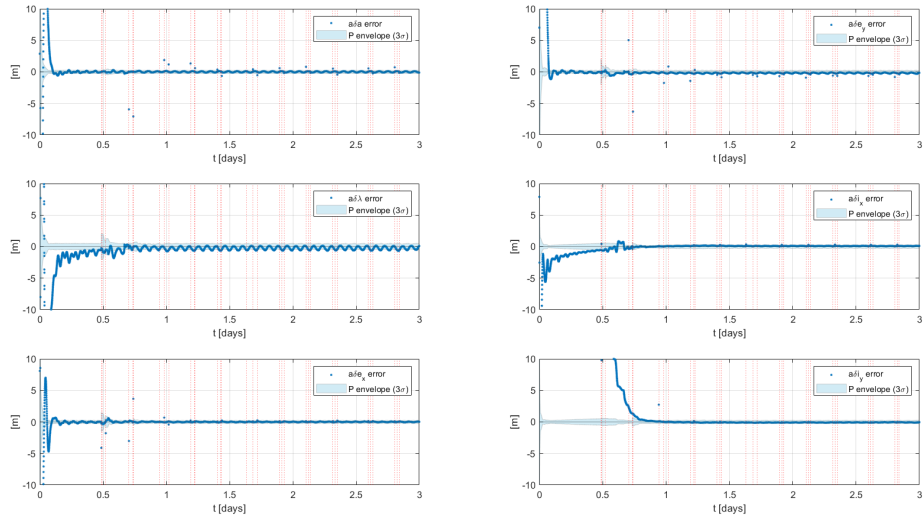


Figure C.3: scenario 02, error

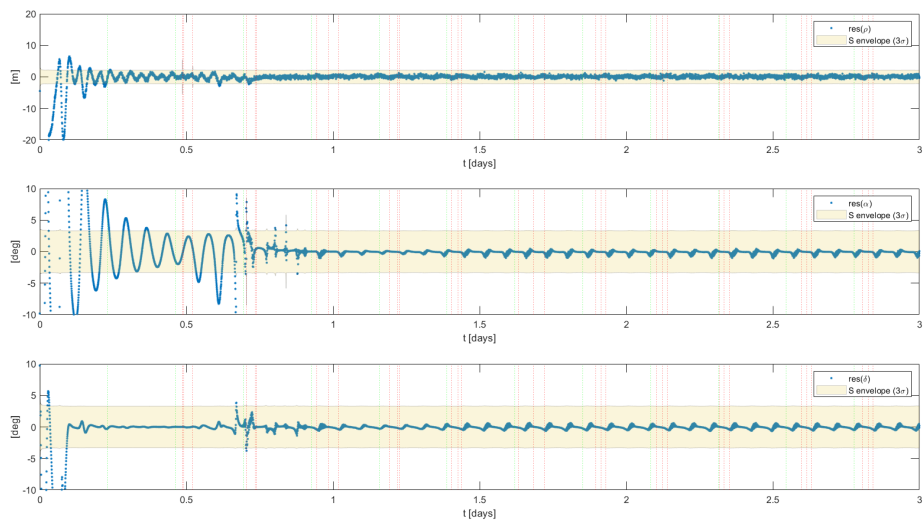


Figure C.4: scenario 02, residuals

Bibliography

- [1] “ESA’s Annual Space Environment Report ESA UNCLASSIFIED-Releasable to the Public,” tech. rep., 2019.
- [2] S. D’Amico, “Autonomous Formation Flying in Low Earth Orbit,” 2010.
- [3] O. Montenbruck and E. Gill, *Satellite Orbits*. Berlin, Heidelberg: Springer Berlin Heidelberg, 2000.
- [4] D. J. Kessler and B. G. Cour-Palais, “Collision frequency of artificial satellites: The creation of a debris belt,” *Journal of Geophysical Research*, vol. 83, no. A6, p. 2637, 1978.
- [5] D. A. Koplow, “Scholarship @ GEORGETOWN LAW Scholarship @ GEORGETOWN LAW ASAT-isfaction: Customary International Law and the Regulation ASAT-isfaction: Customary International Law and the Regulation of Anti-Satellite Weapons of Anti-Satellite Weapons,” tech. rep., 2008.
- [6] B. Weeden, “The Space Debris Created by the Test,” tech. rep., Secure World Foundation, 2010.
- [7] J. Mackey, “Recent US and Chinese antisatellite activities,” p. 12, 2009.
- [8] K.-U. Schrogl, W. Rathgeber, B. Baranes, and C. Venet, “Yearbook on Space Policy 2008/2009: Setting New Trends,” 2010.
- [9] B. Weeden, “The Collision and Resulting Debris,” tech. rep., Secure World Foundation, 2010.
- [10] T. S. Kelso and A. Gorski, “SPACE SURVEILLANCE: LESSONS LEARNED FROM THE IRIDIUM-COSMOS COLLISION,” 2009.
- [11] H. Krag, M. Serrano, V. Braun, P. Kuchynka, M. Catania, J. Siminski, M. Schimmerohn, X. Marc, D. Kuijper, I. Shurmer, A. O’Connell, M. Otten, I. Muñoz, J. Morales, M. Wermuth, and D. McKissock, “A 1 cm space debris impact onto the Sentinel-1A solar array,” *Acta Astronautica*, vol. 137, pp. 434–443, 8 2017.

- [12] H. Klinkrad, “On-orbit risk reduction — collision avoidance,” *Proceedings of the Institution of Mechanical Engineers, Part G: Journal of Aerospace Engineering*, vol. 221, pp. 955–962, 6 2007.
- [13] S. Aida and M. Kirschner, “COLLISION RISK ASSESSMENT AND OPERATIONAL EXPERIENCES FOR LEO SATELLITES AT GSOC,” tech. rep.
- [14] F. Laporte and E. Sasot, “Operational management of collision risks for LEO satellites at CNES,” in *SpaceOps 2008 Conference*, 2008.
- [15] H. Krag, K. Merz, T. Flohrer, S. Lemmens, B. Bastida Virgili, Q. Funke, and V. Braun, “ESA’s Modernised Collision Avoidance Service,” 2016.
- [16] U. Nations Office For Outer Space Affairs, “UNITED NATIONS OFFICE FOR OUTER SPACE AFFAIRS Space Debris Mitigation Guidelines of the Committee on the Peaceful Uses of Outer Space UNITED NATIONS,” tech. rep.
- [17] D. Mehrholz, L. Leushacke, W. Flury, R. Jehn, H. Klinkrad, and M. Landgraf, “Detecting, Tracking and Imaging Space Debris,” tech. rep., 2002.
- [18] S. G. S. J. Fortescue, P. W., “12 Telecommunications,” in *Spacecraft Systems Engineering, Fourth Edition*, ch. 2, p. 724, Wiley, 2011.
- [19] “On the Shoulders of Titans: A History of Project Gemini - Barton C. Hacker, James M. Grimwood - Google Libri.”
- [20] R. W. Fricke, D. W. Camp, D. M. Germany, and L. S. Nicholson, “STS-49 SPACE SHUTTLE MISSION REPORT,” tech. rep., 1992.
- [21] T. Sephton, A. Wishart, K. Strauch, and F. Teston, “EO formation flying applications for small satellite missions,” in *Small Satellites for Earth Observation*, pp. 153–162, Springer Netherlands, 2008.
- [22] P. Bodin, T. Karlsson, R. Larsson, and S. D’Amico, “Prisma Formation Flying Demonstrator: Overview and Conclusions from the Nominal Mission,” *Journal of Guidance Control and Dynamics*, 2011.
- [23] S. D’Amico, J. S. Ardaens, and R. Larsson, “Spaceborne autonomous formation-flying experiment on the PRISMA mission,” *Journal of Guidance, Control, and Dynamics*, vol. 35, pp. 834–850, 5 2012.
- [24] J. S. Ardaens, S. D’Amico, and O. Montenbruck, “Final commissioning of the prisma gps navigation system,” in *Journal of Aerospace Engineering, Sciences and Applications*, vol. 4, pp. 104–118, 7 2012.

- [25] J.-S. Ardaens, S. D'amico, D. Ulrich, and D. Fischer, "TANDEM-X AUTONOMOUS FORMATION FLYING SYSTEM," tech. rep.
- [26] J. S. Ardaens and D. Fischer, "TanDEM-X Autonomous Formation Flying system: Flight results," in *IFAC Proceedings Volumes (IFAC-PapersOnline)*, vol. 44, pp. 709–714, IFAC Secretariat, 1 2011.
- [27] J. S. Ardaens and G. Gaias, "Flight demonstration of spaceborne real-time angles-only navigation to a noncooperative target in low earth orbit," *Acta Astronautica*, vol. 153, pp. 367–382, 12 2018.
- [28] G. Gaias and J. S. Ardaens, "Flight demonstration of autonomous noncooperative rendezvous in low earth orbit," *Journal of Guidance, Control, and Dynamics*, vol. 41, no. 6, pp. 1337–1354, 2018.
- [29] G. Gaias, J.-S. Ardaens, and C. Schultz, "THE AVANTI EXPERIMENT: FLIGHT RESULTS," tech. rep.
- [30] G. Gaias and J.-S. Ardaens, "IWSCFF 17-08 IN-ORBIT EXPERIENCE AND LESSONS LEARNED FROM THE AVANTI EXPERIMENT," tech. rep.
- [31] "VEGA C USER'S MANUAL ISSUE 0 REVISION 0," tech. rep., 2018.
- [32] R. Bate, D. Mueller, and J. White, *Fundamentals of Astrodynamics*. 1971.
- [33] C. J. Cohen and E. C. Hubbard, "A nonsingular set of orbit elements," *The Astronomical Journal*, vol. 67, p. 10, 2 1962.
- [34] H. Schaub, "SPACECRAFT RELATIVE ORBIT GEOMETRY DESCRIPTION THROUGH ORBIT ELEMENT DIFFERENCES," tech. rep.
- [35] G. W. Hill, "Researches in the Lunar Theory," *American Journal of Mathematics*, vol. 1, no. 1, p. 5, 1878.
- [36] W. H. CLOHESSY and R. S. WILTSHIRE, "Terminal Guidance System for Satellite Rendezvous," *Journal of the Aerospace Sciences*, vol. 27, pp. 653–658, 9 1960.
- [37] W. Fehse, *Automated rendezvous and docking of spacecraft*. Cambridge University Press, 2003.
- [38] K. T. Alfriend, H. Schaub, and D. Gim, "Gravitational perturbations, nonlinearity and circular orbit assumption effects on formation flying control strategies," 2000.
- [39] S. D. . Amico, "Relative Orbital Elements as Integration Constants of Hill's Equations," tech. rep.

- [40] “COSPAR INTERNATIONAL REFERENCE ATMOSPHERE (CIRA-2012),” tech. rep., 2012.
- [41] H. Schaub and K. T. Alfriend, “Impulsive feedback control to establish specific mean orbit elements of spacecraft formations,” *Journal of Guidance, Control, and Dynamics*, vol. 24, pp. 739–745, 5 2001.
- [42] J. S. Ardaens and S. D’Amico, “Spaceborne autonomous relative control system for dual satellite formations,” *Journal of Guidance, Control, and Dynamics*, vol. 32, pp. 1859–1870, 11 2009.
- [43] S. D’amico and O. Montenbruck, “Proximity Operations of Formation-Flying Spacecraft Using an Eccentricity/Inclination Vector Separation,” Tech. Rep. 3.
- [44] R. E. Kalman, “A New Approach to Linear Filtering and Prediction Problems,” tech. rep., 1960.
- [45] D. Brouwer, “Solution of the problem of artificial satellite theory without drag,” *The Astronomical Journal*, vol. 64, p. 378, 11 1959.
- [46] M. Rhudy, “Increasing the convergence rate of the extended kalman filter,” in *AIAA Infotech at Aerospace*, American Institute of Aeronautics and Astronautics Inc., 2015.
- [47] D. Simon, *Optimal state estimation: Kalman, H_∞ , and nonlinear approaches*. Hoboken, NJ, USA: Wiley Blackwell, 1 2006.
- [48] M. Willis, K. T. Alfriend, and S. D’Amico, “Second-Order Solution for Relative Motion on Eccentric Orbits in Curvilinear Coordinates,” 9 2019.
- [49] K. T. Alfriend, S. R. Vadali, P. Gurfil, J. P. How, and L. S. Breger, *Spacecraft formation flying: Dynamics, control and navigation*. Butterworth-Heinemann, 2009.